Masteroppgave

NTNU
Norges teknisk-naturvitenskapelige universitet
Fakultet for ingeniørvitenskap
Institutt for maskinteknikk og produksjon

Andreas Malm

Investigating the Effect of Profile Geometry and Gap Tolerances on the Mechanical Response of Thick Section AA6082-T6 Friction Stir Welds for Structural Applications

Masteroppgave i Mechanical Engineering
Veileder: Geir Ringen
Medveileder: Lise Sandnes
Juni 2023

NTNU
Kunnskap for en bedre verden

Andreas Malm

Investigating the Effect of Profile Geometry and Gap Tolerances on the Mechanical Response of Thick Section AA6082-T6 Friction Stir Welds for Structural Applications

Masteroppgave i Mechanical Engineering
Veileder: Geir Ringen
Medveileder: Lise Sandnes
Juni 2023

Norges teknisk-naturvitenskapelige universitet
Fakultet for ingeniørvitenskap
Institutt for maskinteknikk og produksjon

NTNU
Kunnskap for en bedre verden

NTNU
Department of Mechanical and Industrial Engineering

Investigating the Effect of Profile Geometry and Gap Tolerances on the Mechanical Response of Thick Section AA6082-T6 Friction Stir Welds for Structural Applications

Andreas Malm

Master's thesis in mechanical engineering

Submission date: June 2023

Supervisor: Geir Ringen

Co-supervisor: Lise Sandnes

Norwegian University of Science and Technology

Faculty of Engineering (IV)

Department of Mechanical and Industrial Engineering (MTP)

Abstract

Over the next couple of years, major investment will be made to upgrade existing road networks in Norway. One of the possible solutions towards a more and sustainable infrastructure is to replace traditional steel bridges with lightweight aluminium, thus the Alubridge project was initiated back in 2020. The aim of this project is to investigate the possibles for designing and producing large scale aluminium bridges.

In the present work for the Alubridge project, investigation of the effect of profile geometry and gap variances on the mechanical response of extruded thick section (16mm and 22mm) AA6082-T6 Friction Stir Welds (FSW), have been experimented and examined through fatigue and tensile testing, including Digital image correlation (DIC) analysis and fatigue testing of specimens with different gaps of (0, 1, 2) mm.

Based on the same experimental setup as done previously by partners in the Alubridge project. Gap tolerances had no obvious effect on the tensile strength and fatigue life. The fatigue data obtained from the present work, behaves in a similar manner to those previously obtained in the Alubridge project. Results indicate that there was no significant difference in tensile strength between the two joint geometries. However, deformation of the 22mm specimens was observed before the yield stress, its effect on tensile properties appears to be limited.

Preface and Acknowledgments

The present master thesis written during the fall semester 2023 in fulfilment of the MSc degree at the Department of Mechanical and Industrial Engineering (MTP) at the Norwegian University of Science and Technology (NTNU) in Trondheim, Norway.

I would like to thank my supervisor Professor Geir Ringen for his organizing and support. Special thanks to Postdoc. Lise Sandes for her thorough and constructive guidance. It has been a great value for understanding the technology and writing of the report. In addition, I would like to thank all the other individuals who have assisted during the course of the work.

Sammendrag

I løpet av de neste par årene vil det bli gjort store investeringer for å oppgradere det eksisterende veinettverket i Norge. En av de mange mulige løsningene mot en mer bærekraftig infrastruktur er å erstatte tradisjonelle stålbroer med lettvekts- aluminium -broer, dermed ble Alubridge-prosjektet iverksatt i 2020. Målet med dette prosjektet er å undersøke muligheten for å designe og produsere aluminium bruer i stor skala.

I denne master oppgaven for Alubridge-prosjektet, undersøkes effekten av profil geometri og gap-varianser på den mekaniske oppførselen av ekstrudert og friksjonssveiset (FSW), 16mm og 22mm tykk-plate AA6082-T6. Sveisene har blitt eksperimentert og undersøkt gjennom utmatting og strekktesting, inkludert Digital Image Correlation (DIC) -analyse og utmattelse-testing av prøver med forskjellige gap på (0, 1, 2) mm.

Basert på same eksperimentelle oppsett som tidligere gjort av partnere i Alubridge-prosjektet. Gap-toleranser hadde ingen åpenbar effekt på strekk-styrken og utmattelse-levetiden. Utmattelse egenskapene som er hentet fra dette arbeidet, oppfører seg på en lignende måte som innhentet tidligere i Alubridge-prosjektet. Resultatene indikerer at det ikke var stor forskjell på strekkfastheten mellom de to forskjellige prøvegeometriene. Men, deformasjon av 22mm prøvene ble observert før flytespenningen, dens effekt på strekkegenskapene ser ut til å være begrenset.

Table of Contents

List of Figures

List of Tables

List of abbreviations

TWI	The Welding Institute
FSW	Friction Stir Welding
GMAW	Gas Metal Arc Welding
AA	Aluminium Alloy
Mg	Magnesium
Si	Silicon
Al	Aluminium
UTS	Ultimate Tensile Strength
MPa	Megapascal
DIC	Digital image correlation
HAZ	Heat Affected Zone
TMAZ	Thermo-Mechanically Affected Zone
FZ	Fusion Zone
NZ	Nugget Zone
BM	Base Metal
HV	Vickers Hardness

1. Introduction

1.1 Background

Over the next couple of years, major investments will be made to upgrade existing road networks in Norway. As a part of this upgrade, the aim is to replace existing ferry services longside E39 by bridges to focus on sustainable, cost effective and durable solutions. Today, most bridges are fabricated using steel and concrete, which are heavy and require frequent maintenance. One possible solution towards a more sustainable infrastructure is to replace the traditional steel structures with lightweight aluminium.

Today, Al-Mg-Si alloys, such as 6082-T6 are commonly used for statically loaded structures both on and offshore: helicopter decks and living quarters are examples of structures were aluminium has replaced steel, which is the most widely used material for structural applications [1], [2]. Furthermore, these alloys are easily extrudable and thus, an attractive material for new and optimized structural solutions [3], [4]. At present, aluminium is used for shorter and smaller bridges where weight and/or durability is imperative [1]. However, there is a lack of rational design criteria, efficient production methods and reliable durability assessment methods for larger aluminium constructions.

This project was first initiated back in 2020 as a part Norwegian Coastal Highway Route E39 project and is scheduled to run until mid-2023. The aim of the project is to investigate possibilities for designing and producing large scale aluminium bridges in order to reduce travel time and emissions. The specific case that will further investigated is to how to construct an aluminium suspension bridge over Langenuen (located 45 km south from Bergen). This bridge will a total span of 1775 meters, where the goal is that 1250 meters would be made of aluminium.

During the Alubridge project, they decided on the profile geometry, material, and welding methods. They have also undergone fatigue testing on the Friction Stir Welded (FSW) extruded profiles. However, the effect of specimen geometry and gap tolerances have not investigated yet. Extruded aluminium can have various geometrical variations, including dimensional, straightness, twist, and bow variations [1]. The required level of tolerances depends on the intended use of the product – in both AluBridge and FSW – which should be inspected. As previously mentioned, despite the considerable amount of work which has been conducted on the selection of profile geometry, material selection, material testing and proposed welding techniques, some questions remain to be investigated.

First, the selected test geometry of the FS welds is not standardised, and it is therefore not known how it affects the load distribution during testing. Secondly, the effect of gap tolerances on the fatigue behaviour of the FSW is not yet known.

1.2 Objective

This work builds on the previous master thesis of R. Rolle [5] who investigated *Gap Tolerance for Friction Stir Welding of Large, Extruded Aluminium Profiles*. To further investigate the effect of gap tolerances and selected joint geometry designed for Alubridge. The main objectives of the present work can be summarized as follows:

- Investigate the effect of the selected joint geometry on the deformation behaviour of FS welds designed for Alubridge and the effect of different gaps on the deformation behaviour.
- Investigate the effect of gap-tolerances on the fatigue behaviour of FS welds for Alubridge.

1.3 Scope

In this thesis, a more extensive analysis has been conducted on two different sets of FS weld geometries, where one set has a thickness of 16mm whilst the other has a thickness of 22mm. For each of the two sets of weld geometries, FS welds are produced with different gap tolerances (i.e. 0 mm, 1 mm and 2 mm) along the weld seam. To investigate the effect specimen geometry has on the joint deformation behaviour, tensile testing has been conducted and analysed by means of digital image correlation (DIC) technique. Moreover, to investigate the effect of production gap tolerances on the fatigue behaviour of the two sets of FSW welds, high cycle fatigue testing have been conducted.

2. Theory

2.1 Aluminium for structural applications

The unique combinations of properties provided by aluminium and its alloys make aluminium one of most versatile, economical and attractive materials for a broad range of usages [6]. Despite the lower tensile properties to steel, aluminium offers the advantages of high strength-to-weight-ratio and good corrosion resistance which makes them attractive for a variety of structural applications [2].

2.1.1 Classification system of aluminium

In general, pure aluminium is a relatively soft material with low initial strength [7]. Thus, a combination of different alloying elements can be added to improve the properties of aluminium, such as strength, hardness, toughness, and corrosion resistance [7]. Based on the amount and the combination of alloying elements added, different classes of aluminium can be produced.

A variety of different aluminium alloys are commercially available [7]. Based on the type and amount of alloying element they can typically be divided into two categories, cast and wrought alloys. For structural applications, the wrought alloys are most commonly employed [6]. An overview of the general classification system used for wrought aluminium alloys are shown in Figure 1. As seen from the figure, a four-digit numbering system is used to identify different wrought aluminium alloys, whereas the first digit indicates the main alloying element(s) added to the material. Moreover, aluminium alloys strength depends on the element(s) added, which can be further strengthened by heat treatment or work hardening [6].

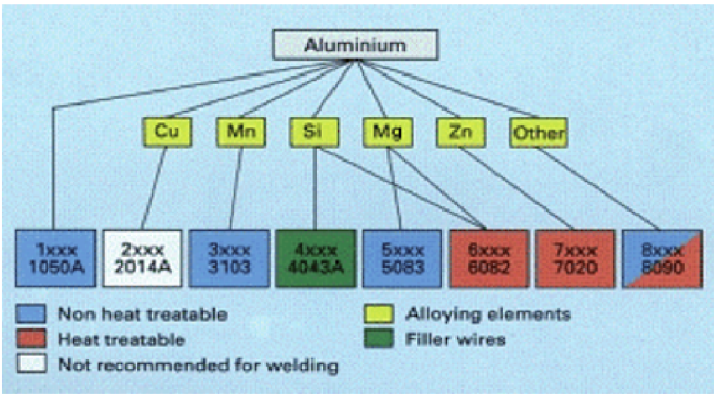

Figure 1: Schematic overview of the general classification system used for wrought aluminium alloys, including the combination of main alloying elements and their strengthening mechanism [8].

2.1.2 Effect of alloying elements on the mechanical properties

The effect of the alloying elements on the mechanical properties are summarised in Figure 2. Among the variety of aluminium alloys available for commercial use, the wrought Al-Mg-Si 6xxx-alloys are commonly used for structural applications [2]. These group of alloys are heat treatable and offer the advantages of medium strength, good formability, weldability, and good resistance against general corrosion [6]. Additionally, the good formability makes Al-Mg-Si alloys suitable for extrusions. As seen in Figure 2 Al-Mg-Si alloys is a medium strength and ductile material. The general mechanical properties range from: Yield strengths of 190-360 MPa and tensile strengths 220-390 MPa with elongation of 17-12% [9]. Alloys in this heat-treatable group may be formed in the T4 temper (solid- solution heat treated without precipitation heat treatment) and strengthened after forming in peak-aged T6 condition by predication heat treatment [6].

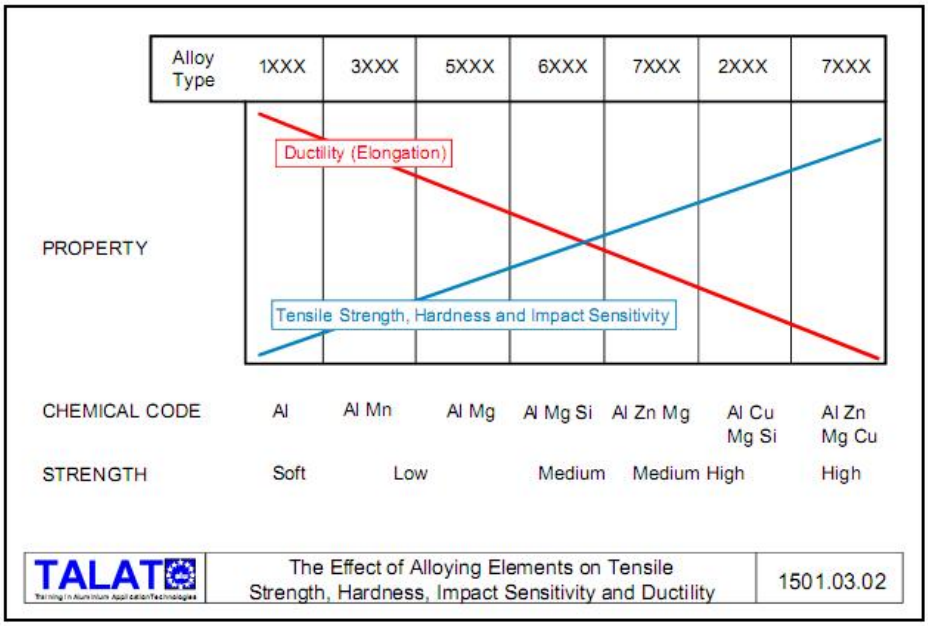

Figure 2: Summarized effects of alloying elements on the mechanical properties of wrought aluminium alloys [10].

2.2 Al-Mg-Si alloys

2.2.1 Main alloying elements

Al-Mg-Si alloys belong to the class of heat treatable wrought aluminium alloys. As such, they obtain their high strength as a result of heat treatment [11]. Their strength is due to the main alloying elements, Magnesium (Mg) and Silicon (Si), which have a significant solid solubility in aluminium. This solubility is utilized during heat treatment to form various hardening phases of Mg and Si, and thus to achieve the desired mechanical properties [12].

Figure 3 shows an overview of the ratio between Mg and Si in some common Al-Mg-Si alloys. The black line in the figure indicates the stoichiometric ratio needed to form Mg_2Si, which occurs during the equilibrium phase [13]. It is important to note, that this phase should not be confused with the meta stable hardening phases that forms during age hardening [14]. Any excess Si, besides the amount needed to form Mg_2Si, contributes significantly to solid solution hardening and thus, increases alloy strength [15].

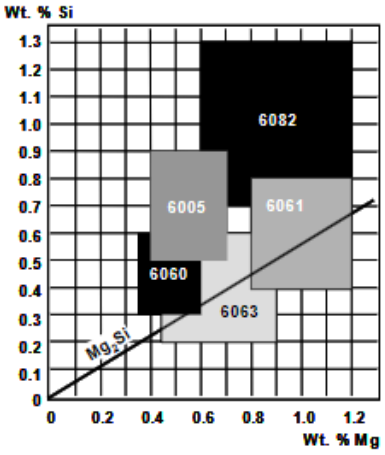

Figure 3: Variation of the main alloying elements in some of the more common Al-Mg-Si alloys [16].

2.2.2 Precipitation hardening

Precipitation hardening, also known as age hardening, is a process used to increase the strength of certain metals and alloys [7]. In the precipitation hardening process of Al-Mg-Si alloys, the material is first heated to a high temperature, typically between 400-500°C, to form a solid solution [12]. The alloy is then rapidly quenched (cooled) to room temperature to freeze the solid solution in place [12]. Next, the alloy is aged at a lower temperature, typically between 120-200°C, for a certain period of time. During this time, the Mg and Si atoms form clusters,

or precipitates, within the aluminium matrix, which strengthen the alloy [17]. This is known as the precipitation or aging stage [17].

The main purpose of solution heat treatment is to ensure that most of the Mg and Si exist in a solid solution within the aluminium matrix, and to provide a homogeneous microstructure [18]. During artificial ageing, the alloy is reheated at a lower temperature [18]. In general, the precipitation sequence for Al-Mg-Si alloys during ageing can be summarized as follows [15]:

$$SS \rightarrow GP - zones \rightarrow \beta'' \rightarrow \beta' \rightarrow Mg_2Si \quad (1)$$

Here, the fine needle shaped β"-precipitates are the dominant hardening phase, where during ageing a high number density of particles are formed uniformly in the matrix [9]. The maximum hardness is obtained when the microstructure consists of both β"-particles and coarser, road shaped, β'-particles [19].

During ageing the material properties constantly change with temperature and time, as illustrated in Figure 4. As apparent the figure, both strength and hardness increase with time, until a peak is reached, i.e., the peak-aged T6 temper condition. Beyond this peak, both strength and hardness decrease with time, as illustrated in Figure 4. It is noteworthy, that solution heat treated Al-Mg-Si alloys has the ability to naturally age by storage at room temperature, as illustrated by the dotted line in Figure 4. This is referred to as the T4 temper condition [20].

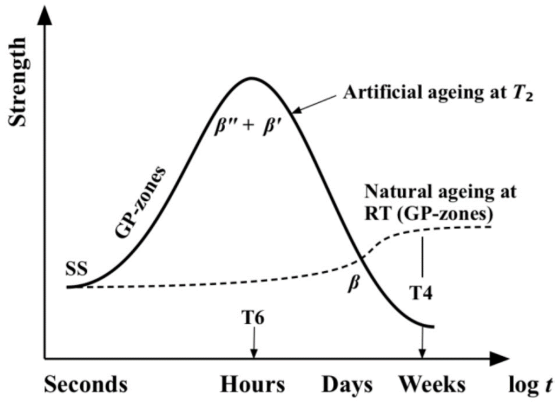

Figure 4: Strength evolution during artificial and natural ageing of Al-Mg-Si alloys [20].

2.3 Production chain

2.3.1 Overview

Al-Mg-Si alloys are typically used in the form of extruded products owing to their good formability in solid solution and the high strength possible to obtain by age hardening [16]. The resulting strength of such extrusions depend on the chemical composition of the alloy as well as the processing conditions throughout the entire production chain [16], [21].

The process chain for fabrication of aluminium extrusions is schematically shown in Figure 5 [16]. The process chain presented in Figure 5(a) is valid for all heat-treatable aluminium alloys, while the temperature profile shown in Figure 5(b) indicates the typical temperatures and times used for extrusion of Al-Mg-Si alloys [16]. All the steps in the process chain (shown in Figure 5) will have an influence on the microstructure of the alloy, and thus the resulting mechanical properties [16], [21].

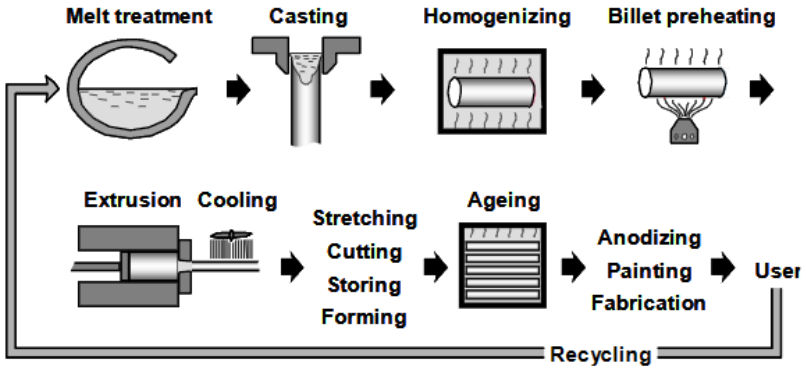

(a)

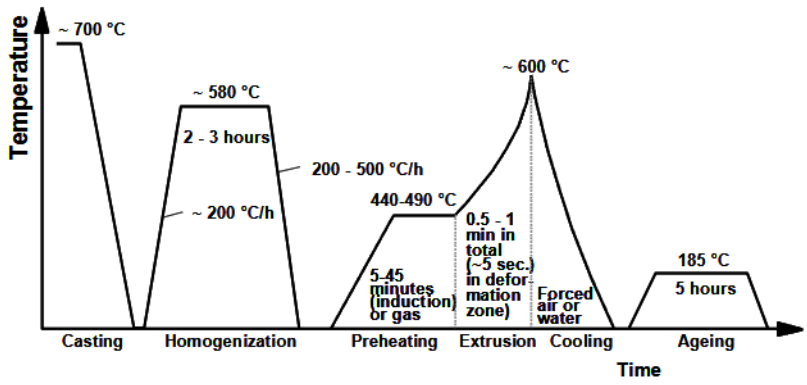

(b)

Figure 5: Schematic illustration of the (a) production chain for producing extruded aluminium profiles and (b) the corresponding temperature/time profile. The time axis is not to scale [16].

The process starts off with the melt treatment. In this step the main alloying elements are added together to the melt with other desirable alloying elements [14]. Thereafter, the molten aluminium is poured into a cooled mould and cast into a billet [21]. After casting, the microstructure of the billet, is quite heterogenous with relatively low ductility [22]. Therefore, homogenization (heat) treatment is necessary to give the alloy maximum precipitation potential before the extrusion [22]. The billet is then preheated for it to be suitable for extrusion. Afterwards the billet is loaded into the extrusion chamber and extruded trough a die, before its rapidly cooled with forced air (fans) or with water [21]. After extrusion, the profile is straightened by stretching, cut into desired lengths, and stored. The extruded profile is artificially aged to obtain maximum strength; the time between extrusion and ageing is normally not controlled and may vary considerably. Anodizing is mainly used for decorative purposes [23]. General mechanical properties of extruded Al-Mg-Si aluminium are shown in Table 1.

Table 1: General Mechanical properties of extruded EN-AW- 6082 Alloy, from NS-EN 755-2 Table 51.

Temper/Profile Geometry	**Thickness, t [mm]**	**Yield Strength [MPa]**	**UTS [MPa]**	**Typical hardness value [HBW]**
T4	< 25	110	205	70
Hollow profile – T6	5 < t < 15	260	310	95

2.3.2 Tolerances

After industrial hot extrusion and subsequent cooling, aluminium profiles are typically distorted, as shown in Figure 6. These distortions may occur due to several factors, including residual stresses, uneven cooling conditions and die wear [24].

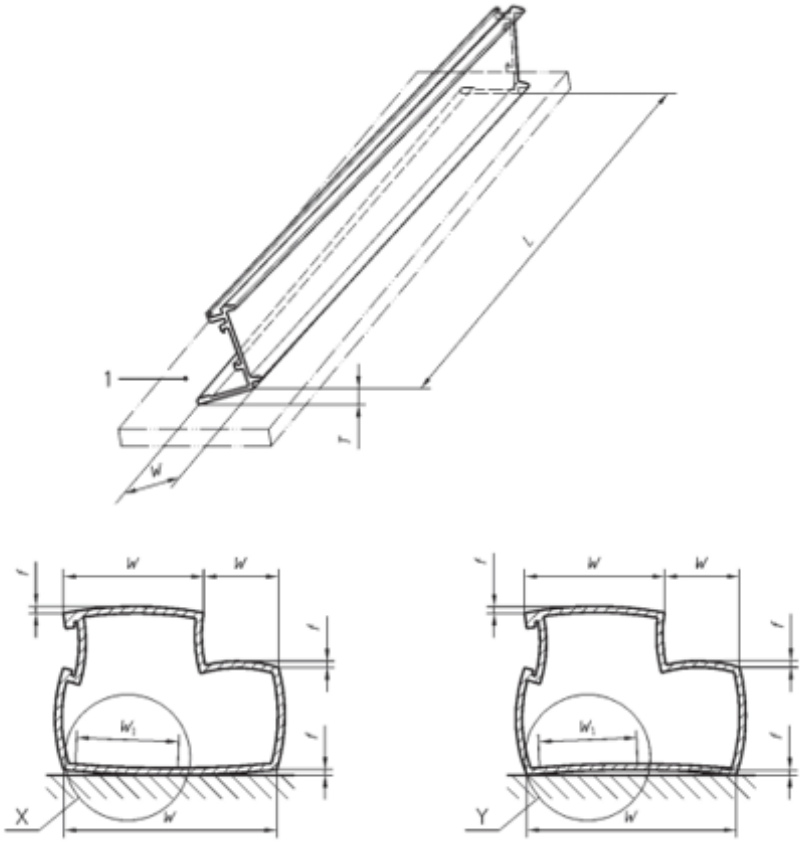

Figure 6: Extruded aluminium can have various geometrical variations, including dimensional, straightness, twist, and bow variations, from NS-EN 755-9.

Post-extrusion techniques, such as stretching are used to reduce distortions and straighten extruded profiles. Distortions can be further minimized by controlling the temperature and cooling rate of the extruded aluminium. High cooling rates can cause severe residual stresses and distortions. However, it is necessary to retain the alloying elements to achieve required mechanical properties and maintain the microstructure of the alloy [25], [26]. This leads to a balance between cooling at rapidly to achieve maximum strength, and cooling slowly to avoid severe distortions [24].

Distorted extruded panels are a challenge for other process further down the production chain [27]. For instance, it effects the stability of the friction stir welding process in presence of

workpiece mating variations, such as gap, mismatch and misalignment. As a result, distortions can significantly affect the weld quality [28], [29]. Figure 7 shows examples of common dimensional and geometrical errors of extruded deck panels.

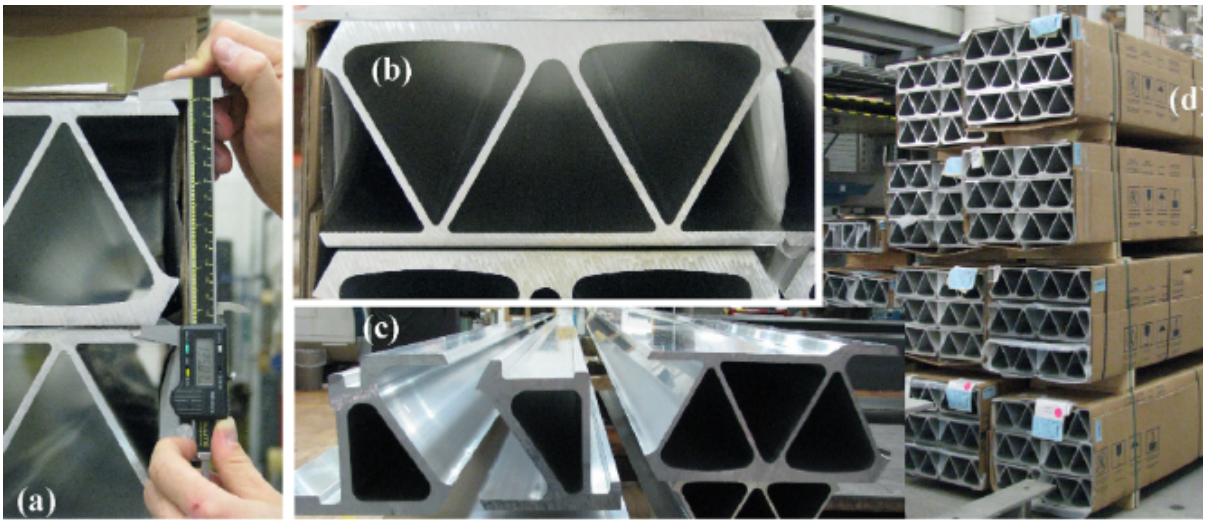

Figure 7: Dimensional and geometrical errors of extruded deck panels. (a) Different height on both profiles, (b) top flatness error, (c) straightness and twist errors, (d) bundles of extrusions as received [1].

2.4 Welding of aluminium alloys

The majority of welding of heat-treated aluminium alloys, like the AA6082-T6, can be welded by a wide variety of fusion welding techniques. The most common methods are gas metal arc welding (GMAW) and gas metal tungsten welding (GMTW) [20]. GMAW is a flexible welding technique that can be used to join a vast number of plate thicknesses and joint geometries. Moreover, GMA welding offers the advantage of high-speed productivity, (i.e. operates at high welding speeds) and operates, at a low cost, as it can be easily mechanized or adapted for robotic operations [6].

Applications of fusion welding may be limited by cracking and degradation mechanisms [20]. Typical problems related to welding of Al-Mg-Si alloys are reduced strength in heat affected zone (HAZ), melt-related defects such as solidification- and hot-cracking, bonding defects, porosity and as-cast microstructure in the fusion zone (FZ) [20].

When it comes to welding of peak aged Al-Mg-Si alloys, the HAZ represent a major problem. The hardening precipitates formed during artificial ageing are thermodynamically unstable [30]. Upon welding, the smallest β''-precipitates will start to dissolve in parts of the HAZ where the peak temperature has been above 250 °C, whilst the largest one will continue to grow. The

hardening precipitates which is closest to the fusion line, experience full reversion of the β''-particles and results in an over-aged condition (see Figure 4, Section 2.2.2). At the same time, the coarser road-shaped β'-precipitates may form in the intermediate peak temperature range between 250 and 450 °C [30], [31]. The effect of welding on the HAZ precipitate evolution is shown in Figure 8.

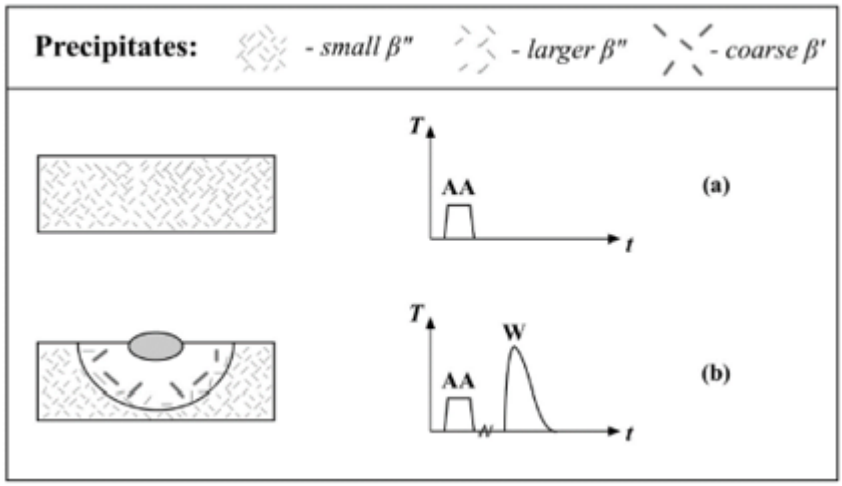

Figure 8: Schematic diagram showing the microstructure evolution during thermal processing of Al-Mg-Si alloys involving heat treatment and welding [30].

GMA welding of peak aged, high strength, Al-Mg-Si alloys (e.g. AA6082-T6) the strength reduction in the HAZ can be as large as 50%. This must be incorporated in engineering design [32]. This strength loss is incorporated in different design codes, for instance Eurocode 9-1:1. The general mechanical properties of AA6082, in addition to strength reduction after fusion welding is as previously mentioned incorporated in design code: Eurocode 9-1:1, - which is presented in Table 2 below [32].

Table 2: Yield Strength and ultimate tensile strength (UTS) before welding, and the strength reduction expected in HAZ after GMAW of AA6082 extruded profiles (EN 755). Eurocode 9-1:1 table 3.2b [32].

Temper	Thickness, t [mm]	Yield strength [MPa]	UTS [MPa]	Strength Reduction Yield Strength [MPa]	Strength Reduction UTS [MPa]
T4	< 25	110	205	100	160
T6	5 < t < 15	260	310	125	185

2.5 Friction stir welding of Al-Mg-Si alloys

Friction stir welding (FSW) is a solid-state joining process invented by The Welding Institute (TWI) in Cambridge, England in 1991 [33]. Since its invention, both research and development have grown exponentially, with many companies, research institutions and universities investing heavily in its process [34], [35]. The major advantages of FSW compared to other welding methods is that it does not involve any material melting, since the temperature is limited to about 80% of the melting temperature of the base material. Moreover, FSW does not require the use of any shielding gas, nor does it need a filler metal [36]. Hence, melt-related defects and the as-cast microstructure associated with the fusion zone (FZ) is eliminated [37]. All commercial aluminium alloys can be joined by FSW, including high-strength aluminium alloys (2xxx- and 7xxx-series) that are susceptible to solidification cracking in the fusion zone [34]. The process is also able to weld dissimilar materials, such as different series of alloys or different materials [34].

2.5.1 Working principles

The main principles of FSW are illustrated in Figure 9. As is apparent from the figure, a rotating tool is vertically inserted into two abutted sheets or plates before it horizontally transverses along the contact surface. Subsequently, the sheets or plates can be joined by the stir behaviour of the tool. The rotation of the tool serves a dual purpose; generating heat and transferring metal. As the tool rotates on the surface, frictional heat is created, causing the material to ‘soften’ and deform plasticly. The softened material is constrained by the tool shoulder. As the tool moves along the joint line, plasticized material is swept around the pin to form a solid phase joint behind the tool [37]. The side of the weld where the tool rotation-direction is similar to the welding direction is called the advancing side (AS), while the opposite side is called the retreating side (RS). At the end of the weld line the tool is retracted, leaving a hole at the end of the weld.

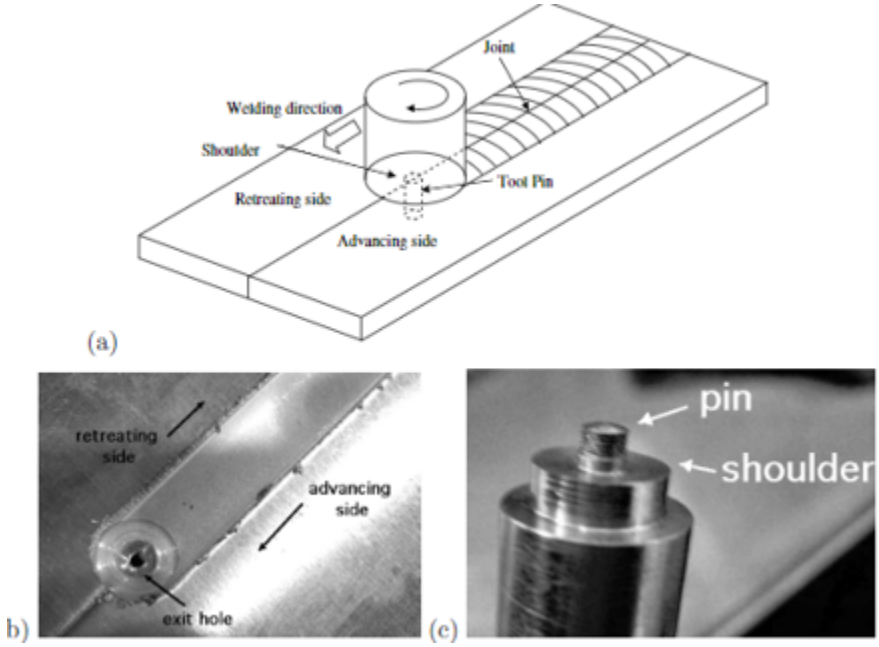

Figure 9: (a) Schematic illustration of the FSW process, (b) an FS weld between two abutting aluminium sheets, (c) FSW tool [38].

Due to the fully mechanized nature of the welding process, it is easy to repeat. It consistently delivers high-quality welds, with only a few variables need to be monitoring; tool-type, feeding rates, rotational speed and position [39]. FSW is also a flexible process, that can be applied to join butt, lap and spot weld geometries, as shown in Figure 10. The FSW of fillet joints, as shown in Figure 10(g), are difficult to weld as there is no filler material added during welding.

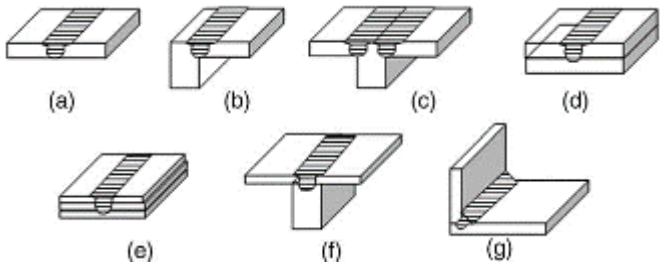

Figure 10: Joint configurations for FSW: (a) square butt, (b) edge butt, (c) T butt joint, (d) lap joint, (e) multiple lap joint, (f) T lap joint, and (g) fillet joint [40].

2.5.2 Microstructure and strength

The microstructure of the FSW joint depends on various parameters, including the welding parameters, tool design and materials to be joined [41]. Generally, the microstructure consist of four different microstructural zones with different material flow patterns and associated temperature changes [40]. These are the nugget zone (NZ), thermo-mechanically affected zone (TMAZ) and the HAZ, and the unaffected base material (BM), as shown in Figure 11.

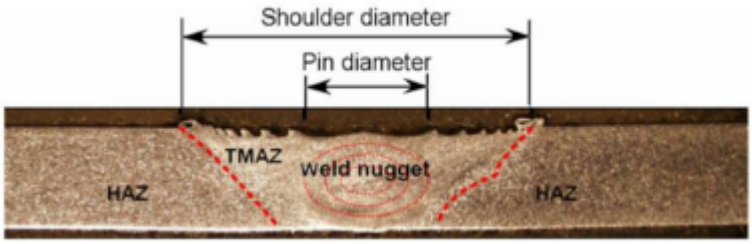

Figure 11: Classification of various regions in a FSW of AA6061-T6 [42].

In the NZ ("weld nugget" from the figure above) the tool has stirred the material and created a new microstructure. The material in this zone experiences significant plastic deformation and recrystallization. Hence, it is often identified as the dynamically recrystallized region [37]. The thermo-mechanically affected zone (TMAZ) ends at the FSW-tool-shoulder, determined by the dashed lines [42]. TMAZ has been plastically deformed by the FS-tool, and heat from processing has affected the material without recrystallization [37]. Adjacent to the TMAZ, the heat affected zone (HAZ) appears. In this zone, there are no obvious changes to the microstructure. However, this region has been significantly affected by heat from the FSW process, effectively altering the precipitation hardening state. Al-Mg-Si alloys in the T6 temper are particularly prone to softening in the TMAZ/HAZ interface, as the heat generated during welding affects the precipitation hardened structure. This causes hardness and strength to be significantly lower compared with the base material in this region [37], [31], [43]. Figure 12 illustrates typical hardness evolution of an Al-Mg-Si FS welded joint.

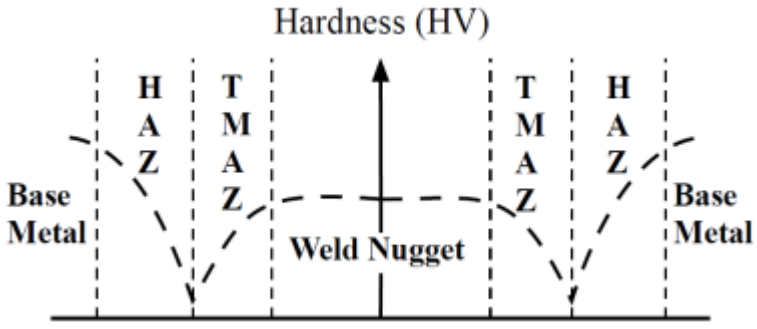

Figure 12: Illustration of typical hardness evolution of FS joint [43].

2.5.3 Comparison to traditional welding

Previous data indicate that tensile strength and fatigue performance of FSW of aluminium alloys joint is usually stronger than a fusion weld [39], [44], [45]. In FSW, the extent of the heat-affected zone (HAZ) and the resulting loss in strength is comparatively lower to other traditional welding methods such GMAW. This is primarily due to the absence of melting [40]. Hence, melt-related defects and the as-cast microstructure associated with the fusion zone (FZ) are eliminated [37]. In addition, the lower temperature reduces distortion and residual stress [46]. The resulting geometry in the weld region of FSW has no material build-up compared to that of GMAW. Local geometry of welds, such as sharp transitions, melt-related defects and different bonding defects, cause local stress concentrations at the joint [47]. Depending on the type of loading, these defects can play a key role in the starting point of fatigue crack initiation [48]. Characteristic visual differences of FSW and GMAW are shown in Figure 13.

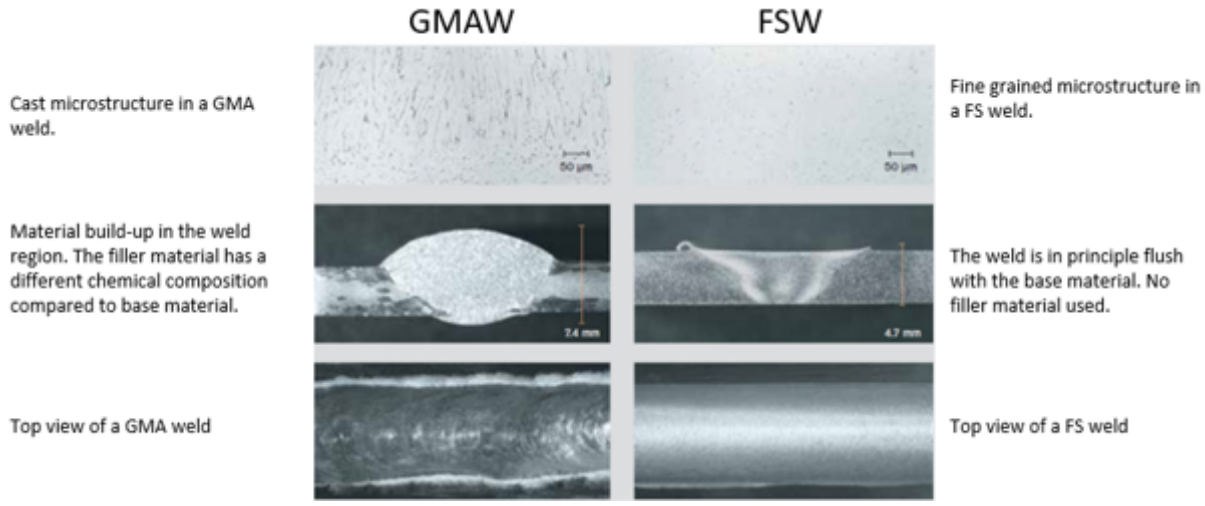

Figure 13: Characteristic visual differences of FSW and GMAW are shown from three different perspectives: Microstructure, cross-section and top view [39].

2.6 FSW of thick sections

2.6.1 Methods and approaches

Today, FSW is typically used for industrial joining of aluminium plates in the thickness (<10 mm) [37], [40]. However, for structural applications, using a more robust FS-tool and fixtures enables the joining of thicker plates/profiles as well. The forces involved in moving the tool through the material to be joined are considerable. Thus, to control and ensure high quality welds the FSW equipment must be sturdy. This necessitates strong backing, fixation (for handling and adjusting for tolerances) and a rigid machine [39]. FS welding of thick plates can be done either from one side, as previously shown in Figures 10, or by conducting double-sided FSW, as shown in Figure 14. FSW demonstrates a high joint completion rate when dealing with thicker materials, as welds can be successfully accomplished in a single pass. In contrast, other welding processes which may need multiple weld-passes over the weld seam. Therefore, even though welding speeds are lower, the joint completion rate is higher for thick plate welding[49], [50].

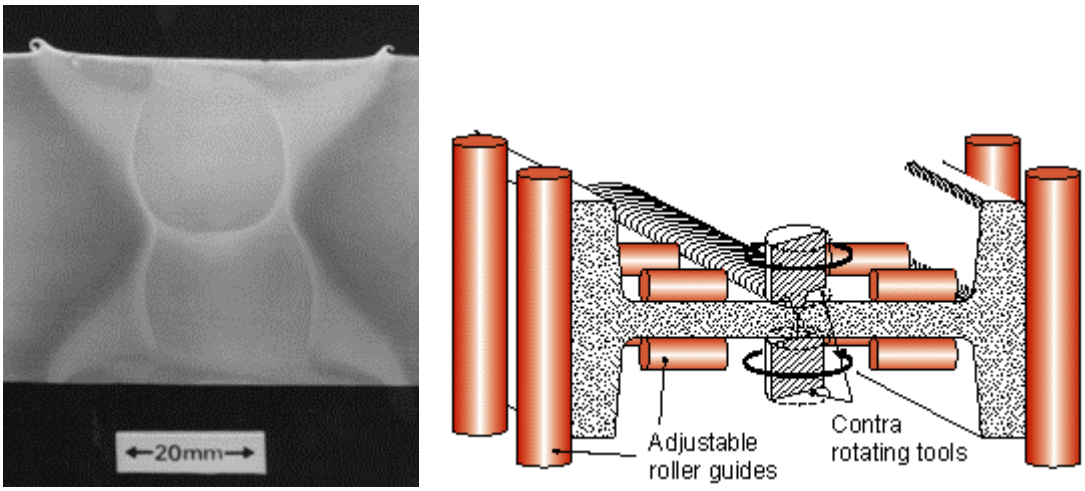

Figure 14: (left) Transverse microsection of FS welded AA6082-T6 50mm plate from both sides [36]. (right) illustration of double sided welding operation with contra rotating tools and roller fixtures [50].

2.6.2 Preliminary literature review of FSW of thick sections

At present, little external information regarding the mechanical properties of thick section weldments has been provided to the AluBridge project. Thus, as a possible contribution to the project, a collection of existing data regarding thick plate welding has been collected and structured by means of scientific literature. The literature utilized in this section consist of data collected during the pre-master report, spring semester 2022. The collected research papers consist of various topics within the FSW process. However, focus has been limited to FS

welding of Al-Mg-Si alloys having a thickness larger than 9 mm. A variety of researchers have reported data for other alloys [40], [46], [51].

The reported literature data found for thick section FSW of Al-Mg-Si alloys are summarised in Table 3. From this, it appears that the scientific literature regarding this topic is rather limited in scope. Whilst the exact reason for this gap- in the -literature remain unknown, it may be due to the difficulty in welding thick section Al-Mg-Si profiles. Additionally, making high quality welds require high forces and expensive equipment. A secondary explanation could be that the use of thick section aluminium profiles for practical applications are limited. The production conditions for FS welds, and whether they are produced under industrial conditions or under laboratory conditions, are also unknown.

In the data collected in Table 3, there seems to be little difference in the obtained UTS with respect to plate thickness. In addition, the reported relative hardness ($\frac{HV_{Weld}}{HV_{BM}}$) appears to be reduced with increasing plate thickness over (t > 10mm). For the FS weld with 42mm the hardness appears to increase again. However, this specific weld is of a double-sided FSW-tool, which may affect the heat distribution in the joint compared to single-sided FSW. At present there is little external literature information the fatigue behaviour of thick plated aluminium alloy sections.

Table 3: Included in the table is both the base metal (BM) used, the plate thickness (t), the base material hardness (HV_{BM}), the minimum hardness of the weld (HV_{Weld}), relative hardness (HV_{Weld})/(HV_{BM}), the applied welding speed (v), the applied pin rotation (RPM), the base metal and weld tensile strength (UTS_{BM} and UTS), and the source of the data. All hardness data are Vickers hardness.

BM	**t [mm]**	**(a)HV_{BM}**	**(b)HV_{Weld}**	**Relative HV [b/a]**	***v [mm/min]***	**Pin rotation [RPM]**	**UTS_{BM} [MPa]**	**UTS [MPa]**	**Source**
6061-T6	9.4	95	65	0.68	400	1200	280	232	[45]
6082-T6	20	140	70	0.50	350	500	-	225	[51]
6061-T6	20	-	-	-	200	400	-	-	[52]
6082-T6	25	105	55	0.52	300	400	330	-	[53]
6061-T6	25.4	110	57	0.51	408	480	-	235	[54]
6082-T6	42	100	60	0.6	110	400	-	225	[31]*

*Double-sided FSW.

3. Alubridge

3.1.1 Material, extrusion design and welding

Since the beginning of the AluBridge project back in 2020, several design solutions based on aluminium extrusions and alloy alternatives have undergone evaluation [55]. Figure 15(a) shown an illustration of the Langenuen bridge. Figure 15(b) shows the current proposed design solution for the bridge girder. Where the overall dimensions of the bridge girder cross section are 34m x 5,5m. The bridge girder will be constructed by assembling multiple smaller AA6082-T6 extruded profiles, specially designed for the purpose. The concept involves assembling the profiles into larger panels using FSW, with a final dimension of 12m x 3,09m. Subsequently, the on-site assembly will be carried out using GMAW.

(a)

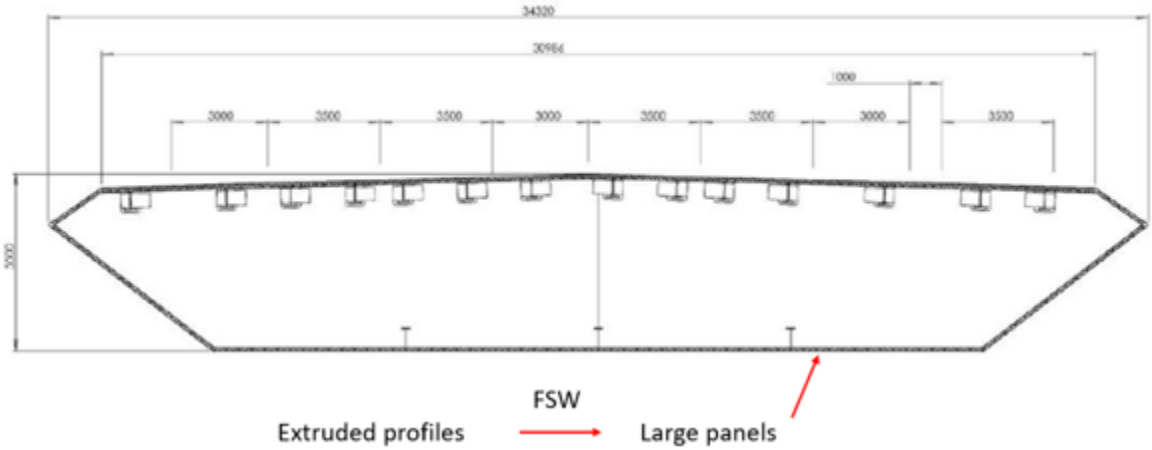

(b)

Figure 15: (a) Illustration of Langenuen bridge [56], (b) Cross-section view of proposed design solution of bridge girder, the bridge girder will be constructed by assembling multiple smaller AA6082-T6 extruded profiles, the concept involves assembling the profiles into larger panels using FSW [55].

The exact geometry of the extruded profiles have not yet been decided. Currently, two different joint geometries for the FSW are proposed, both of which are incorporated into a single profile, as shown in Figure 16, (red arrow represent the FS weld locations). In the upper part of the profile, the material thickness is 16 mm in around the weld (Design 1), while in the lower region the thickness is increased to 22 mm (Design 2).

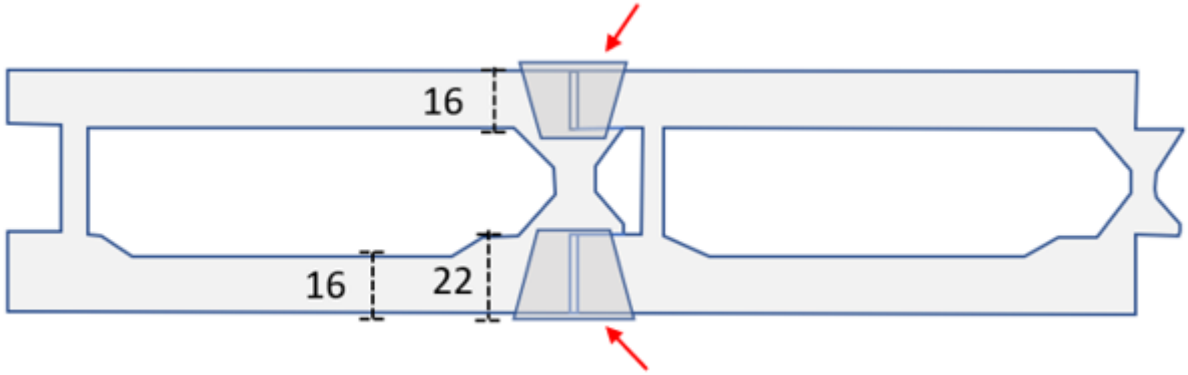

Figure 16: Cross-section view with thickness dimensions [mm] of two abutting extruded profiles, (red arrows) marks the location of two FS welds from top and bottom.

3.1.2 Current status on material testing

The present work and testing in this thesis follow the same experimental setup, based on work done previously by NTNU, Hydro, and Sintef in the Alubridge project. Evidently, both GMA and FS welded joints have been tested under fatigue loading. From this, it is indicated that both welds are capable of reaching fatigue strength levels that makes them suitable for dynamically loaded structures (L. Sandnes, Personal communication, 2023). Figure 17 and Figure 18 show testing results of the two weld joint designs (L. Sandnes, Personal communication, 2023). The black line is based on Eurocode 9 design curve of Fatigue class 32-3,4 for fusion welding as there is no current standard for FSW.

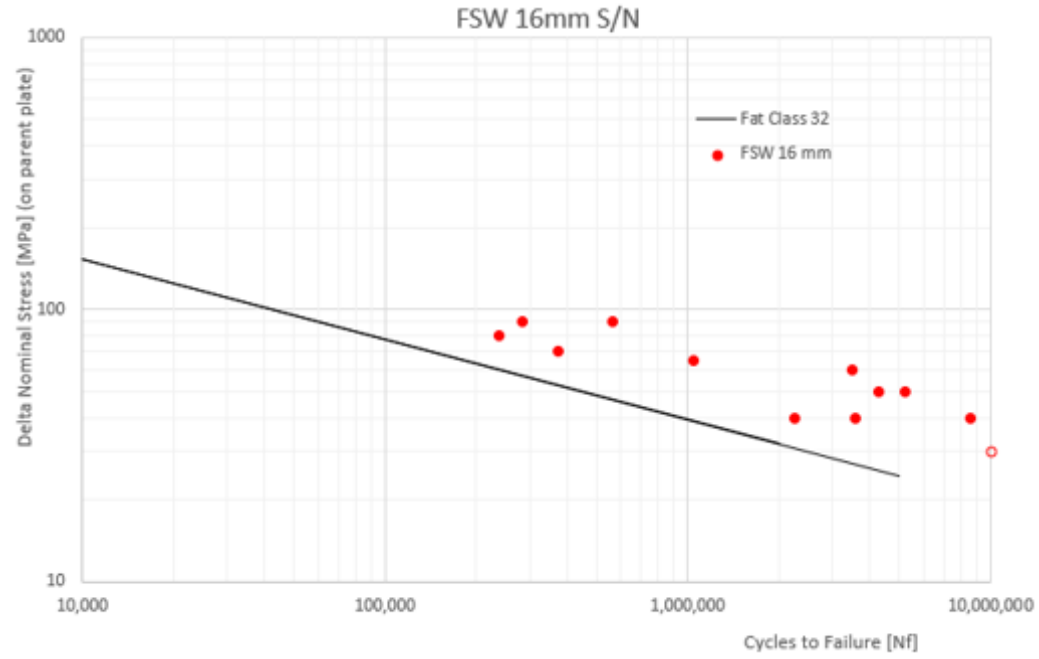

Figure 17: Fatigue testing of 16mm specimen, hollow marks are fatigue run out tests. Performed by partners in Alubridge.

There were less fatigue tests done on the 22mm weld design as it was observed that fracture occurred in the base material and not in the weld region.

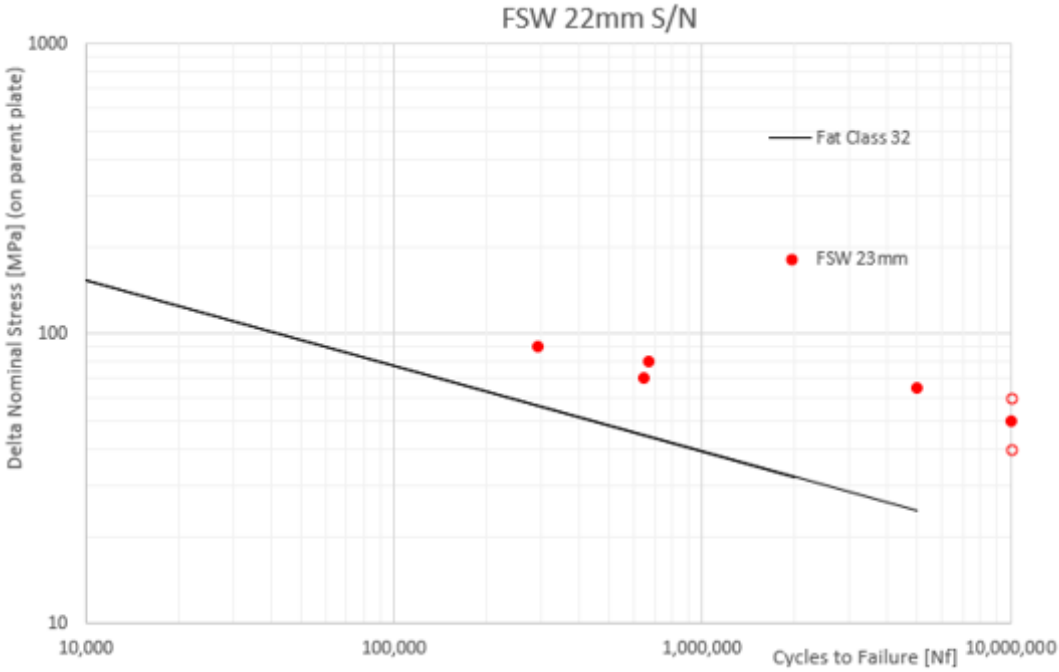

Figure 18: Fatigue testing of 22mm specimens, hollow marks are fatigue run out tests. Performed by partners in Alubridge.

3.1.3 Challenges related to FSW for large span bridges

When it comes to FSW of thick section profiles for industrial use in the Alubridge project there exist several challenges. Up until now, the FS welds that have undergone testing, has been fabricated under optimal laboratory conditions Here, the welded profiles have been relatively short, with a total length of 1 m [5]. In an industrial setting, the joined profiles would be much longer (up to 12 meters as previously mentioned 3.1.1) and a wider variety of challenges are thus more likely to occur.

For instance, as-extruded aluminium profiles are normally not straight and have varying tolerances along the profile, which can significantly influence the weld quality in the structure of the bridge. Moreover, the profile variations would be larger for long extrusions [1]. This may cause fluctuating variations along the profile during FSW, which could give rise to insufficient bonding along the joint line [27].

Studies indicate that if gap between abutted plates exceeds a certain gap, it would significantly reduce the weld quality [28], [29]. Cole et al. performed tests on 5mm thick AA5083. Abutting plates having a 1.5mm gap (25% of pin diameter, 30% of BM) would cause 20% reduction in UTS, and gap of 2mm would produce voids in the weld joint [29].

Ma et al. reports the effect if gaps upon join quality and thermometrical behaviour of 6.2mm 2A14-T6 aluminium alloy with butt gaps of 0.8mm, 1.6mm, 2mm [28]. As indicated by the fracture properties of tensile specimens, it expressed varied characteristics with the different gaps. FS welds without metallurgical defects were obtained up to gaps of 0.8mm, with kissing bond and void defects at 1.6mm, followed by tunnel defects for 2mm gap. Joint efficiency, decreased slightly (0.73 to 0.71) from 0 to 0.8mm gap. However, joint efficiency decreased sharply (0.63 to 0.43) from 1.6 to 2mm gaps [28].

3.1.4 Previous work on gap tolerances

Currently, there is limited understanding on the capability of the FSW process capability to handle variations along the weld line, particularly when it comes to joining thick section products. However, R. Rolle in 2022, conducted a preliminary study on the effect of gap tolerances on the FSW process for Alubridge [5]. In his work, a systematic investigation on the effect of increasing gaps in FS welding between the two joint designs, for both the 16mm and 22mm joint thickness as intended for Alubridge. As shown in Figure 19, macrographic weld cross-sections of the two designs with gaps of 2 to 3mm. Design 1, Figure 19(16mm) are of 16mm weld sections, whilst Design 2, Figure 19(22mm) are of 22mm weld sections. The macrographic examination was performed using standard procedures at Hydro Innovation and Technology in Finspång, Sweden [5].

Based on this study, it was discovered that, on a macroscopic level, it is possible to produce defect free FS welds with a gap up to 2 mm. This finding was supported by tensile testing which showed little variation in UTS for specimens with 2 mm gaps. UTS of 16mm was about 239 $\pm$ 2 MPa while UTS of 22mm was about 232 $\pm$ 2 MPa. The highest overall deviance between gapless- and 2mm gaps -welds was a decrease of 1.3% in UTS.

16mm 2Gap

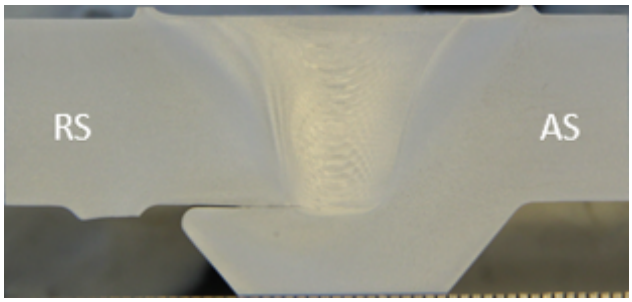

16mm 3Gap

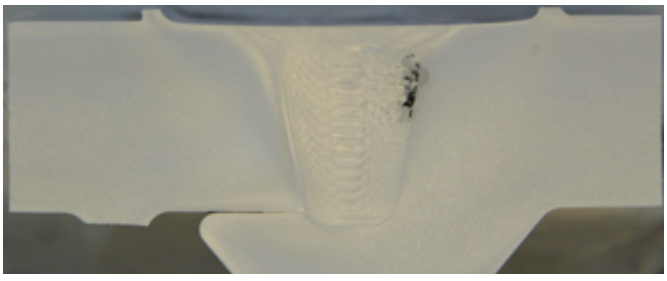

22mm 2Gap

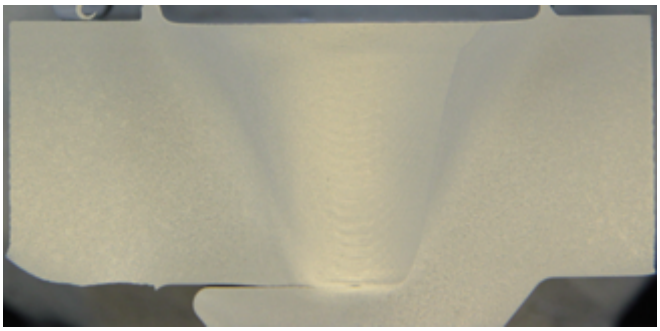

22mm 3Gap

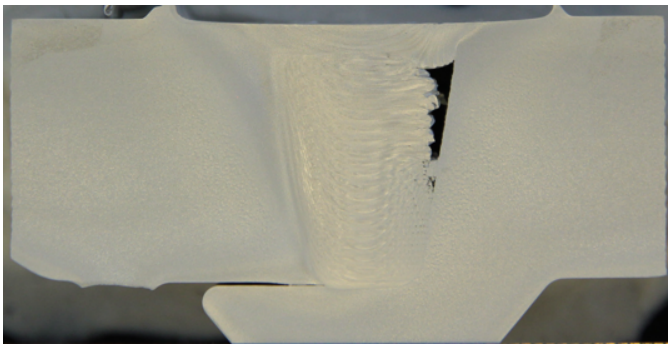

Figure 19: Macrographic images of weld cross-sections at different gaps for Design 1 of 16mm, Design 2 of 22mm (R.Rolle, Personal communication, 2023).

4. Experimental

4.1 Material and profile geometry

4.1.1 Chemical composition

The aluminium alloy used for the experimental work in this thesis is AA6082-T6. The chemical composition of this alloy can be seen in Table 4 below.

Table 4: The chemical composition of the aluminium alloy AA6082-T6

Alloying element (wt%)										
Si	Fe	Cu	Mn	Mg	Cr	Ni	Zn	Ti	Pb	Al
0.95	0.19	0.03	0.49	0.61	<0.01	<0.01	0.01	0.01	<0.01	Bal.

4.1.2 Extrusion

The material was cast, homogenized, and extruded using industrial standards at Hydro in Finspång, Sweden. For research purposes, a scaled down deck profile was used in this study, as can be seen in Figure 20.

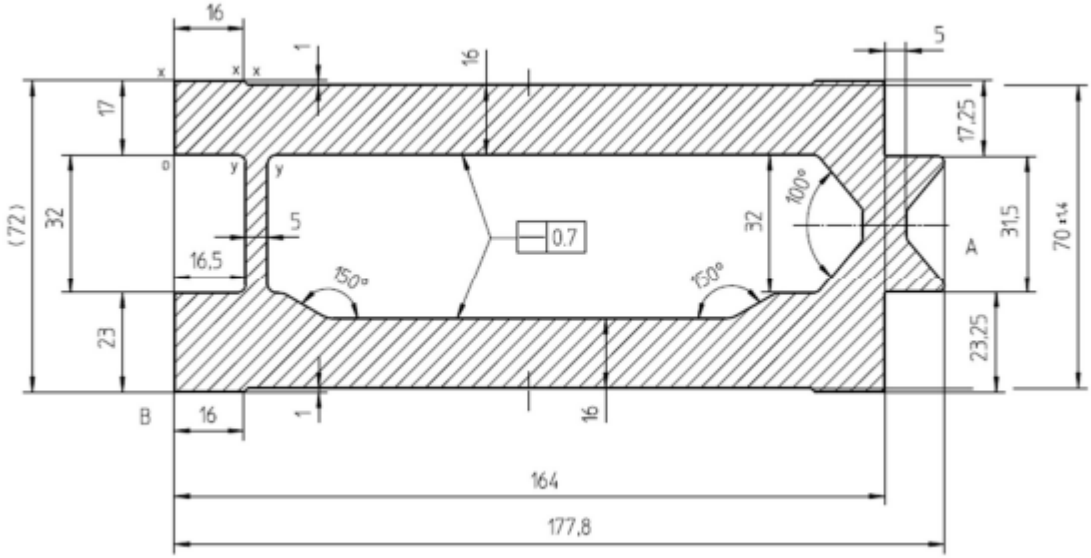

Figure 20: Cross section and dimensions of resulting extruded profile.

4.1.3 Welding conditions

The FSW was performed with an MTS I-STIR PDS FSW machine at Hydro Innovation and Technology in Finspång, Sweden. The welding process of these profiles were observed by Robert Rolle. From his work: fit-up, welding, and post-weld, were discussed together with the results of the macrographic cross-sections with relation to the forces and torques during welding. The parameters and procedures which were utilized during welding were generated

from the company's internal knowledge of the FSW process. The welding parameters were kept constant to isolate and analyse the effect of gaps have on weld quality. Due to confidentiality, the specifics are not discussed within this thesis.

The joining of two profiles resulted in a 1-meter-long butt joint on either side of the profile. Top butt-joint at 16mm wall thickness and bottom joint at 22mm respectively. Gapless joints, followed by artificial gaps of (1, 2, 3) mm along the weld-joint were created using steel spacers at each end of the weld. No spacers were added in the middle since using an aluminium spacer would result in its consumption during the welding process. This would not have represented a realistic scenario during production, and the added material would influence the results [5]. Figure 21 shows the fixture setup for welding the 1-meter length profiles. Welding direction is the same as extrusion.

(a)

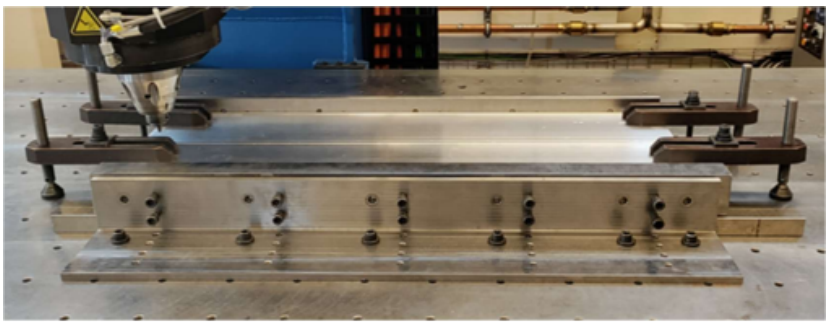

(b)

Figure 21: Fixture setup, with steel spacer at the start of the weld seam (marked with red arrows) (a), fixture setup with FS-tool (b) (R.Rolle).

4.2 Sampling area and test matrix

The cross section of the profiles was cut as indicated by the red lines in Figure 22, separating the two weld sections.

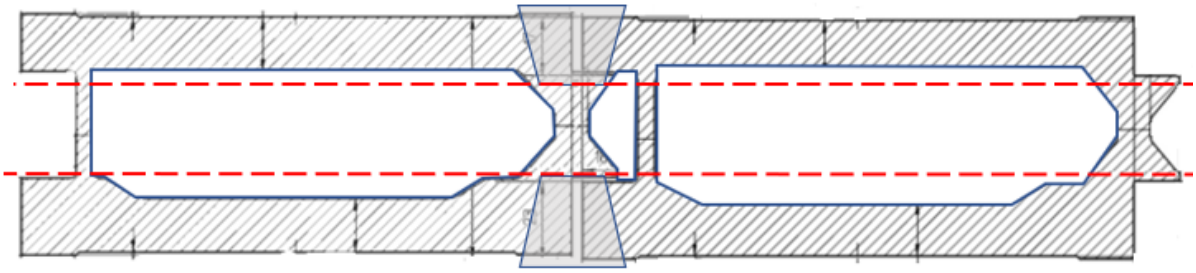

Figure 22: Cross section of welded profiles, red lines indicates whereas profile is cut.

From the initial 1-meter length of the profiles, the start and stop of each weld were removed at 140mm from each edge of the weldment. The plate was then cut into two parts, separating the start and end of the weld, as shown in Figure 23. To support his work, R. Rolle used the end-plates for tensile testing. The testing in this thesis are performed on the start-plates of the weld, which is marked red in Figure 23.

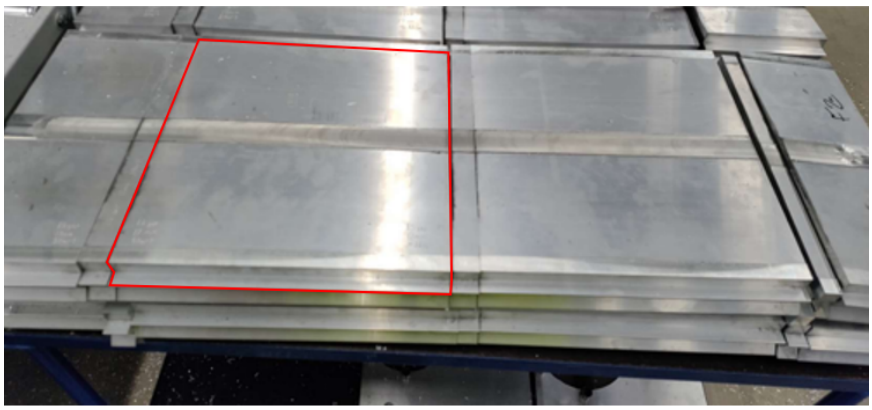

Figure 23: The profiles was cut into two parts, welding direction from left to right (R.Rolle).

As is apparent from Figure 24, each section was CNC machined and cut into four tensile specimens. Unfortunately, the grip length that was machined out, was insufficient for the available tensile testing machine grippers. Therefore, this length was extended as indicated by the dashed lines in Figure 24.

The end pieces (marked *0 and 0*) are dummy-pieces used for trial-testing. Table 5 show an overview of the available test samples. 3mm gap joints were discarded due to visible bonding defects [5]. From this table, the samples are sorted into DIC tensile samples and fatigue samples.

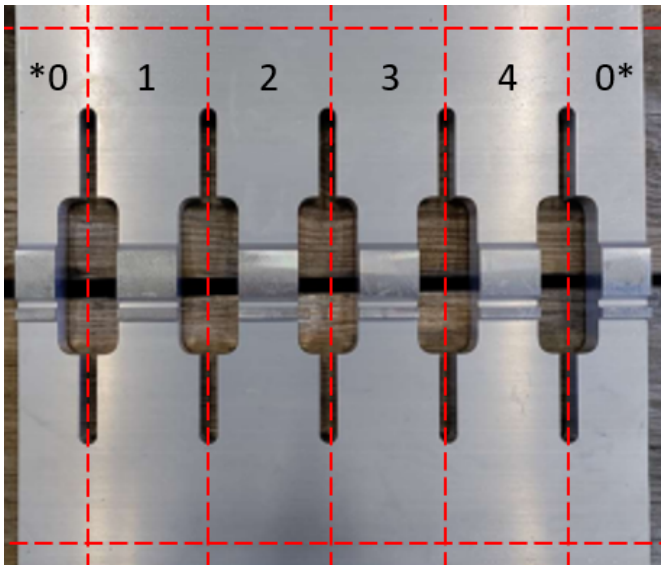

Figure 24: CNC machined tensile test specimens, dashed lines indicated whereas length was extended and cut.

Table 5: Overview of available test samples

Thickness/Gap [mm]	0 mm	1 mm	2 mm	Total
16 mm	4	4	4	12
22 mm	4	4	4	12

4.3 Tensile testing

The specimens were tested at the Fatigue Lab at MTP with a Instron – 8854 Axial- torsion test machine equipped with a load cell of 250KN, with crosshead speed set to 0.9 mm/min. This corresponds to a nominal strain rate of $1.5 \cdot 10^{-3}\ s^{-1}$.

4.3.1 Specimen geometry

An illustration of the two-weld section designs are shown in Figure 25. Meanwhile, drawing and dimensions are provided in the appendices (see Appendix A). From the figure, both specimens have the same gauge length of 60mm. The 22mm weld design have a nominal plate thickness of 16mm, which is increased to 22mm in the weld region by the apparent geometrical transition located close to the grip/head of the specimen.

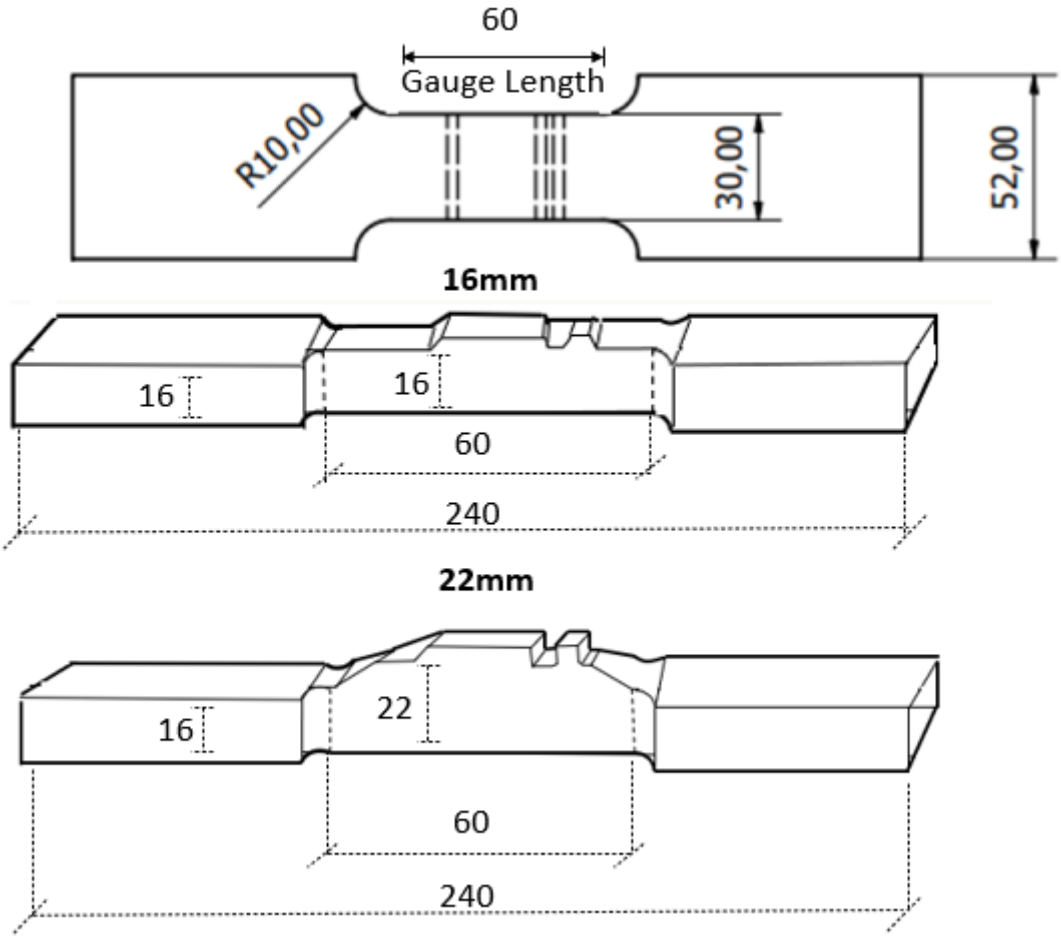

Figure 25: Illustration of the two-weld section designs.

4.3.2 DIC

Digital image correlation (DIC) is a non-contact strain measuring technique with a wide range of applications [57]. It has been used to measure and analyse the evolution and uniformity of strain in material testing, in crack tip and crack propagation studies, to detect damage development and structural deflections, high temperature strain mapping and dynamic vibration analysis [57].

In its basic form two-dimensional DIC can be viewed as a "point tracker", i.e an algorithm that tracks the translation of a specific point (speckles) on the surface of a plane specimen in a series of images. The translation of the speckles is found by comparing an image of the current (deformed) state of an image to the image reference state [58]. A high-resolution camera is used to capture images of a fine-grained speckled pattern on the material surface at different intervals during testing. These images are analysed with a specialised post-processing software to determine the displacement and deformation of the surface [59]. A typical setup for two-dimensional DIC is illustrated in Figure 26.

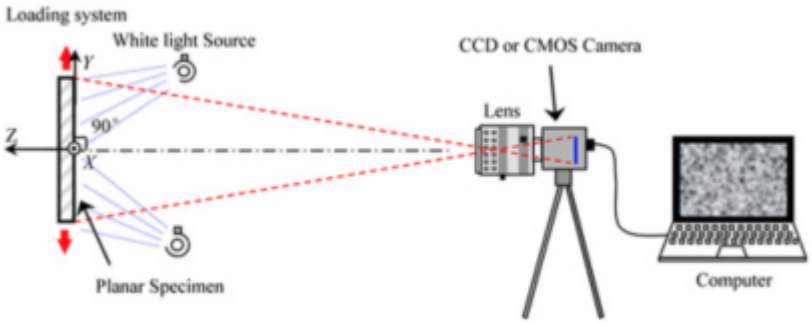

Figure 26: Illustration of two-dimensional DIC setup [59].

A two-dimensional DIC analysis was carried out to record the strain evolution that occurred in the weld zone during tensile testing. This experimental DIC tensile testing was conducted together with SINTEF at the Fatigue lab at MTP. A total of five tests were conducted using different gaps as shown in Table 6.

Table 6: DIC Tensile test matrix

Thickness/Gap [mm]	0 mm	1 mm	2 mm	Total
16 mm	1	0	1	2
22 mm	1	1	1	3

One important consideration when conducting DIC-testing is to ensure that the surface is properly prepared to avoid any interference with the image analysis. Therefore, the surface was spray-painted white, to remove the reflection of the metallic surface and to enhance the contrast (T. Kristensen, personal communication, 2023 SINTEF). Then, the surface was sprayed half a meter apart with black paint, creating a thin, random fine-grained speckled pattern on the surface, as shown in Figure 27.

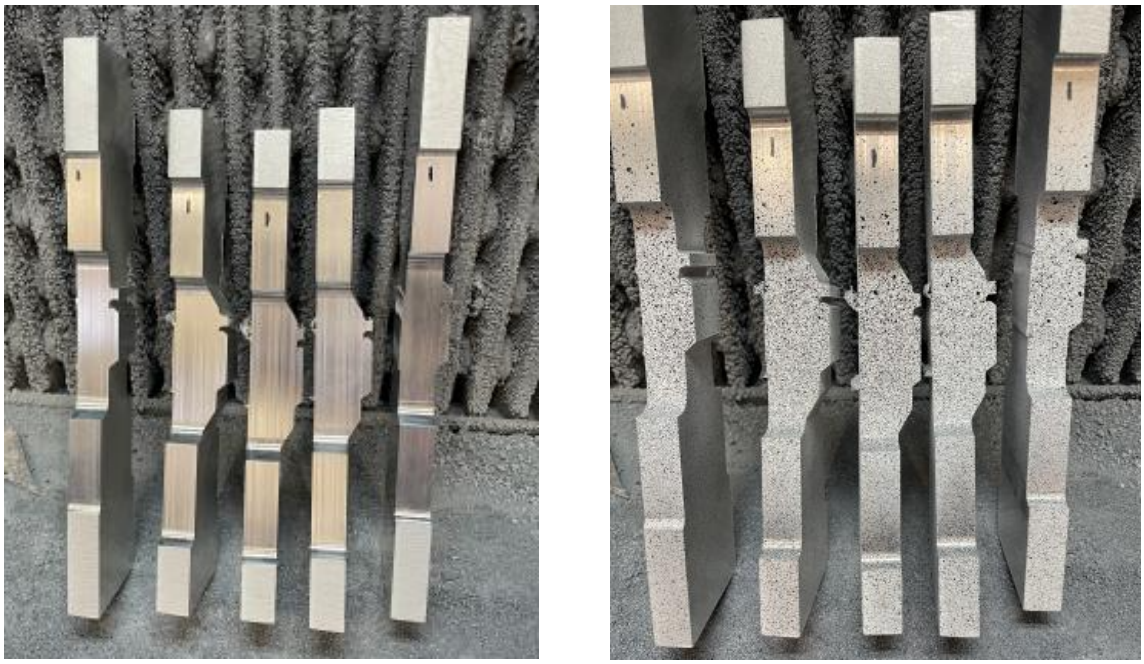

(a) (b)

Figure 27: Clean specimens before spaying (a), specimens after white spray coating and black spray paint to create speckle pattern (b).

Thereafter, a high-resolution camera as well as, a mirror with subsequent lighting was employed to monitor the changes in the pattern that occurred during deformation. It is imperative that the surface and camera are perpendicular and levelled to avoid interference (T. Kristensen, personal communication, 2023 SINTEF). Moreover, due to space considerations, the mirror was necessary to achieve plane images. The mirror was an external reflective film mirror, as to avoid interference with the glass. The distance from camera to the centre of the mirror was 430mm, following 120mm to the material surface. Between 1400 and 2200 images was recorded per test, this test setup is shown in Figure 28.

Figure 28: Test setup showing the camera (1), the mirror (2), and the light source (3).

The subsequent post-processing of the data was done by employing the software eCorr developed by Egil Fagerholt [58]. In the software, quadratic mesh with an element size of 25 x 25 pixels, is added to a reference image taking prior to testing, which then is projected onto the stored images taken during loading. From this the strain evolution of the weld-zone can be captured and presented in the form of two-dimensional field maps. In addition, virtual extensometers (vectors), with a gauge length of 55.5 mm, are projected onto the mesh to extract numerical displacement data needed for the strain analysis. Figure 29 show images of the reference images in the post-processing software with mesh and virtual extensometers.

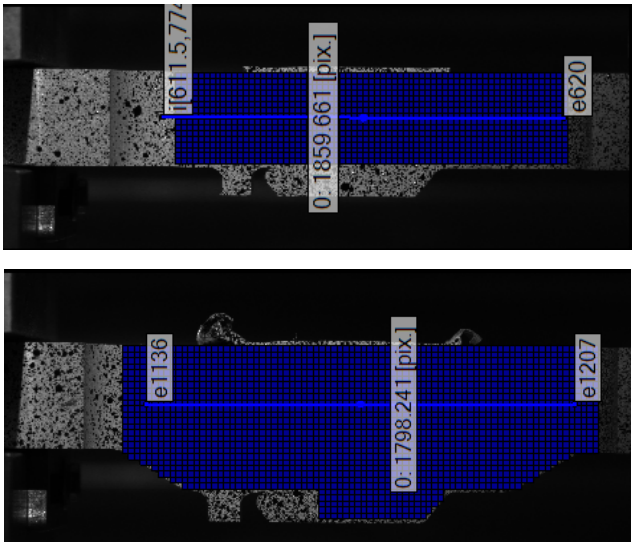

Figure 29: Post processing with mesh and virtual extensometer on (top) 16mm specimens, (bottom) 22mm specimens.

4.4 Fatigue testing

Constant-amplitude axial fatigue tests were carried out using a sinusoidal load time mode at a fixed stress ratio of $R = 0.1$. The tests were conducted in room temperature (RT) with surface finish as received, after machining. The specimen's geometry was the same as the tensile specimens tested with the same testing machine: Instron – 8854 Axial-torsion testing machine, equipped with a load cell of 250KN, operating at 15 Hz. The fatigue life of the specimens were defined by the number of cycles, to complete failure, at a given stress range. In cases where test failure did not occur, the test run-out condition were set to $4 * 10^6$cycles, (which none of the tests excided). The limiting factor of this testing campaign was time. The hydraulic testing machine had a capacity of 15 Hz, with limiting booking time.

To support the previous work by NTNU, Hydro, and SINTEF, the specimens were tested with stress ranges of $\Delta\sigma_{nom} = 90 - 60\ MPa$, to obtain data in the range of $10^5 - 4 \cdot 10^6$ cycles to failure. The maximum applied stress of was 48KN, (about 42% of UTS). A total of 19 fatigue tests were conducted, with different gaps as shown in Table 7. Details of the applied loads for each stress range of the specimens can be found in Appendices (See Appendix B).

Table 7: Fatigue test matrix

Thickness/Gap [mm]	0 mm	1 mm	2 mm	Total
16 mm	3	4	3	10
22 mm	3	3	3	9

5. Results

5.1 Tensile test results

A stress-strain plot from the tensile results is shown in Figure 30. The stress-strain plot was obtained by calculating engineering stress based on the logged force and area of the welded cross sections of (16 x 30 mm^2) and (22 x 30 mm^2). In addition to the percent strain of the virtual extensometers (55.5mm) from the DIC post-processing. The calculated yield and UTS for all specimens tested can be found in Table 8. As is apparent from analysing the plot and from Table 8 below, there is little variation in yield strength and ultimate tensile strengths between the two joint designs. From this small testing size, Design 1 (16mm), obtains higher yield stress values than Design 2 (22mm) and a small amount of higher UTS. Design 2 obtains higher strain values, however, the most likely reason for this outcome may be the different testing geometry. Gap tolerances had little to no effect on the UTS between the samples.

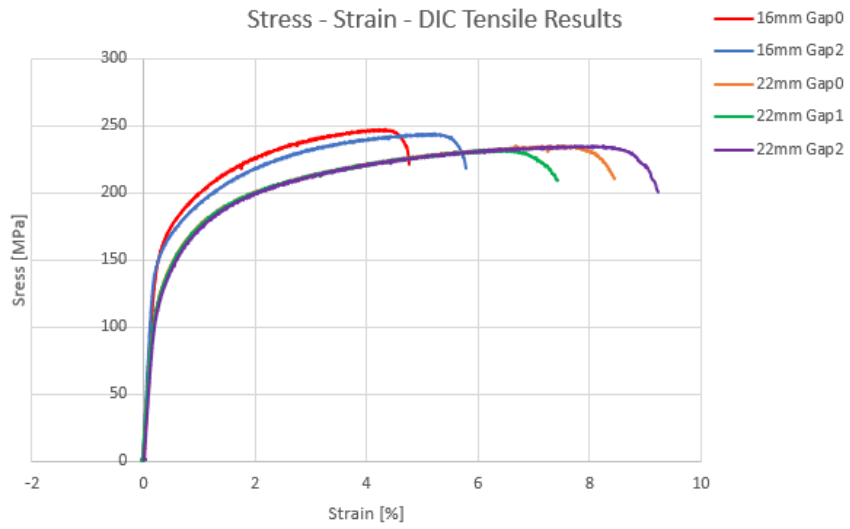

Figure 30: Stress - strain plot of DIC Tensile testing results of both specimen geometries.

Table 8: Included in the table are the (ID) of tensile specimens, the 0.2% yield strength, ultimate tensile strength (UTS), strain in % at UTS, and E-module.

ID	0.2% Yield strength [MPa]	UTS [MPa]	Strain – UTS [%]	E-module [GPa]
16mm – 0Gap	170	246	4.3	60
16mm – 2Gap	165	242	5.2	60
22mm – 0Gap	140	234	7.8	62
22mm – 1Gap	140	231	6.7	62
22mm – 2Gap	140	234	8.0	62

5.2 Fracture examination

5.2.1 16mm

After tensile testing all specimens were visual examined and pictured. Figure 31 shows macro fracture images of 16mm specimens. Fracture occurred within the HAZ. However, this is to be expected as the strain typically localise in the soft area of the HAZ in welded joints. From Figure 31(b) highlighted red at the bottom the weld, there are signs of incomplete bonding, and from Figure 31(a) it appears that this unbonded region has contracted more than the rest of the component. The weld root flaw of the unbonded region can be avoided by slightly increasing the FS-tool pin length [37].

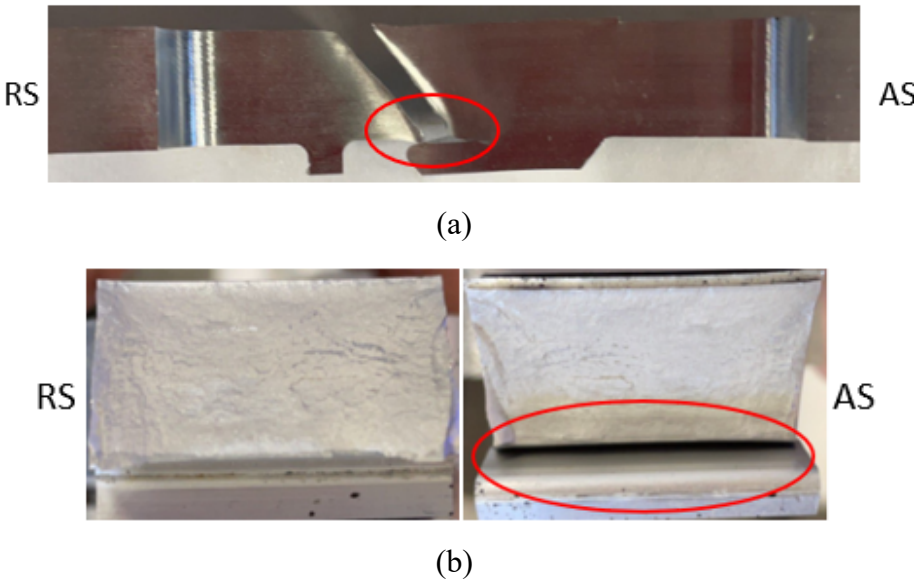

Figure 31: Macro fracture images of 16mm 2Gap specimen, transverse image of fracture (a), image of fracture surface (b). Area marked in red indicates sign of incomplete bonding.

5.2.2 22mm

Figure 32 shows the macro fracture images of 22mm specimens. There are considerable amounts of strain localization within the HAZ, similar to the 16mm specimens. However, the fracture is quite different with respect to 16mm specimens. It appears that during tensile testing the fracture had changed course towards a typical shear fracture which propagates into the initial profile thickness. Likewise, the tensile testing had given rise to bending moment in all the 22mm specimens, as the specimens were deformed and bended. Similar unbonded area with respect to 16mm specimens is observed at the bottom of the weld.

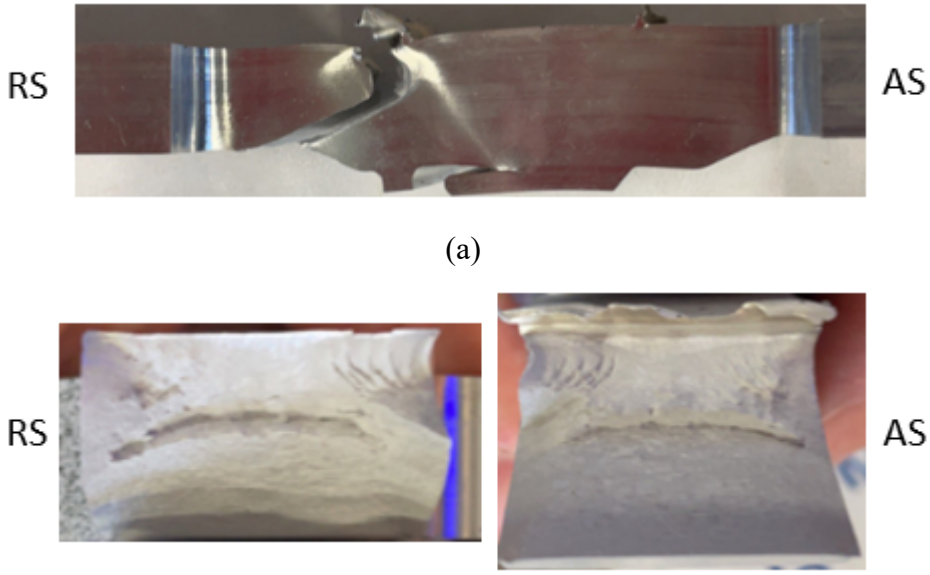

Figure 32: Macro fracture images of 22mm 2Gap specimen. Transverse image of fracture shows change in fracture orientation (a), fracture of surface is uneven after change in fracture orientation (b).

5.3 DIC analysis

5.3.1 16mm

The series of images in Figure 33 shows the evolution of the principal strain (ε_{p1}): at yield strength (1), UTS (2), and strain at fracture (3), for the 16mm specimens. Both specimens deform in a similar matter, whereas most of the strain localized within the HAZ at the retreating side (RS). The unbonded region (marked in red) opens and meets the lower region of HAZ. The fracture has the displacement of a typical shear fracture. Results show that fracture starts in the top region of the HAZ and propagate towards the unbonded region. From the principal strain field maps (field map scales are different): Total ε_{p1} at yield stress of 0.020, UTS ε_{p1} of 0.24, with ε_{p1} of 0.40 at fracture. When the gap between the profiles increases, notch size increased as well (marked with yellow lines). However, the difference in notch size had no obvious effect. Gap tolerances had no obvious effect on the strain evolution between the specimens.

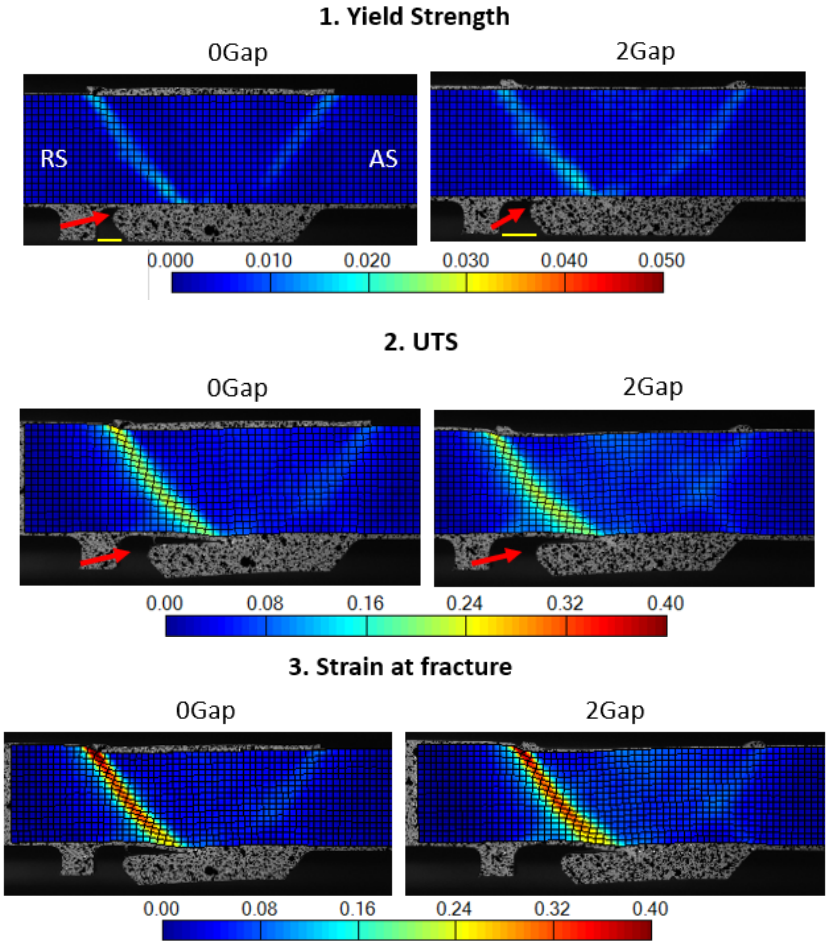

Figure 33: DIC field map images of principal strain of 16mm specimens. Includes is field map scale bars of the strain values. Note that different scalebars are used in the three cases.

5.3.2 22mm

Figure 34 shows the evolution of the principal strain ε_{p1} at yield strength (1), UTS (2), and strain at fracture (3), for the 22mm specimens. Larger images are provided in the Appendices (See Appendix C). Opposed to the 16mm specimens, at yield strength (1), the strain localizes only at the top of the HAZ and at the geometrical transition from initial base plate thickness to the weld section (highlighted by red circle).

Similar to the 16mm specimens, the unbonded region opens and meets the HAZ on the RS. However, as the strain on the RS accumulates, signs of bending are observed and is indicated by the deformation of the mesh at the UTS (2). From the displacement caused by the bending, tension forces accumulate at the top of HAZ and at the geometrical transitions. With further deformation, crack initiation was observed at the geometrical transition at AS for 0- and 1-mm gaps and at RS for 2mm gaps. The fractures (3) propagate towards the thicker material towards the HAZ at the top of the weld. One should note that other cracks may have propagated outside the scope of the two-dimensional DIC imagery.

From the ε_{p1} field maps (field map scales are different): total ε_{p1} at yield stress of 0.020, UTS ε_{p1} of 0.35, with ε_{p1} of 0.40 at fracture. Similar to the 16mm specimens, notch size increase with increasing gaps between the profiles. However, the difference in notch size had no obvious effect. Gap tolerances had no obvious effect on the strain evolution between the specimens.

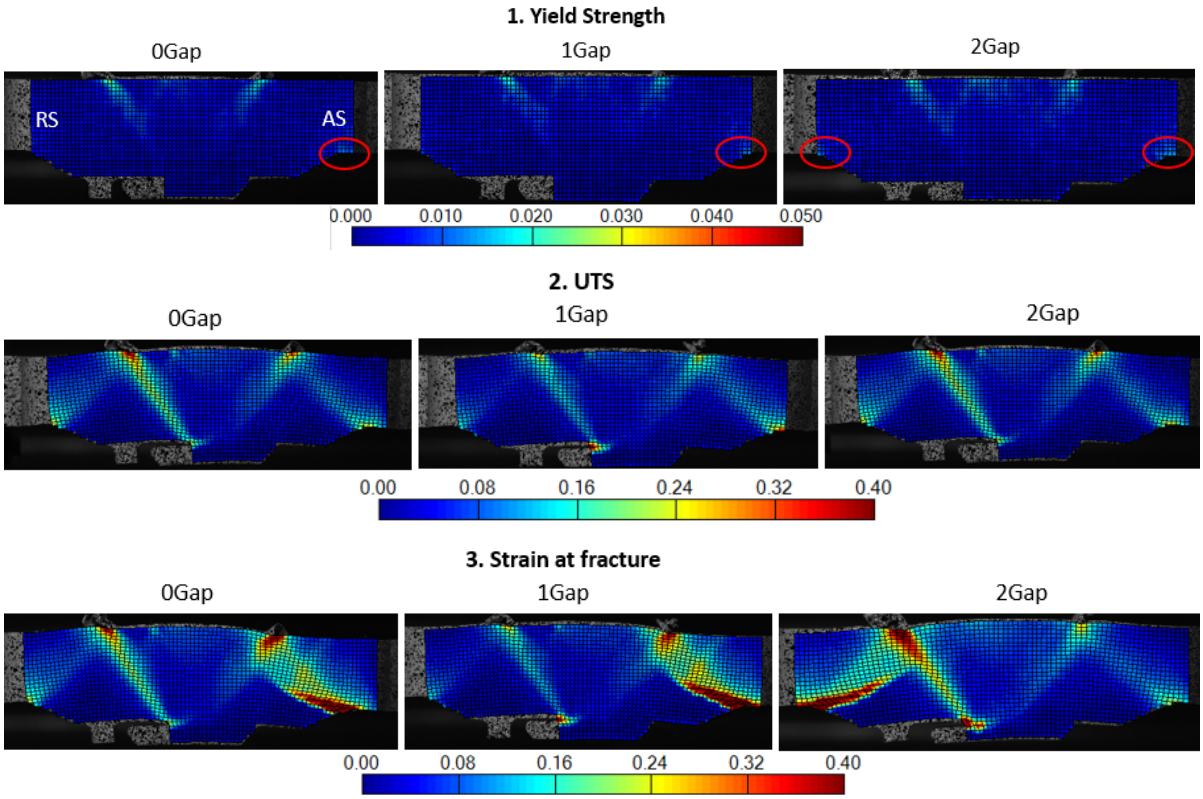

Figure 34: DIC field map images of principal strain of 22mm specimens. Includes is field map scale bars of the strain values. Note that different scalebars are used in the three cases.

5.4 Fatigue test results

Figure 35 and Figure 36 show the fatigue test results, where the S-N curve is presented on the form:

$$\log_{10} N_f = A + B \cdot \log_{10} \Delta\sigma \qquad (2)$$

Where *Nf* is the number of cycles to failure, $\Delta\sigma$ is the nominal stress range of the applied stress amplitude, while A and B are curve fitting constants. The linear regression analysis was conducted with accordance to ASTM standard E739-10(2015) [60]. Table 9 summarises the calculated values for the constants A and B used in Eq. (2). Area sections used to obtain stress values are (16 x 30 mm^2) for both sets of specimens, as tests were done previously in the Alubridge project.

Table 9: Included in the table are the calculated values for the constants A and B used in Eq. (2). Values calculated with accordance with ASTM E739-10(2015) [60].

Type of specimen	A	B
16 mm	13.93	- 4.33
22 mm	18.55	- 6.74

5.4.1 16mm

Figure 35 shows the fatigue testing results of the 16mm specimens, with the mean linear regression line. From this gaps of 0mm tend to have general higher values than 2Gap, and 1Gap has a small amount above the average. However, there are far too few tests for statistical generalisation [61].

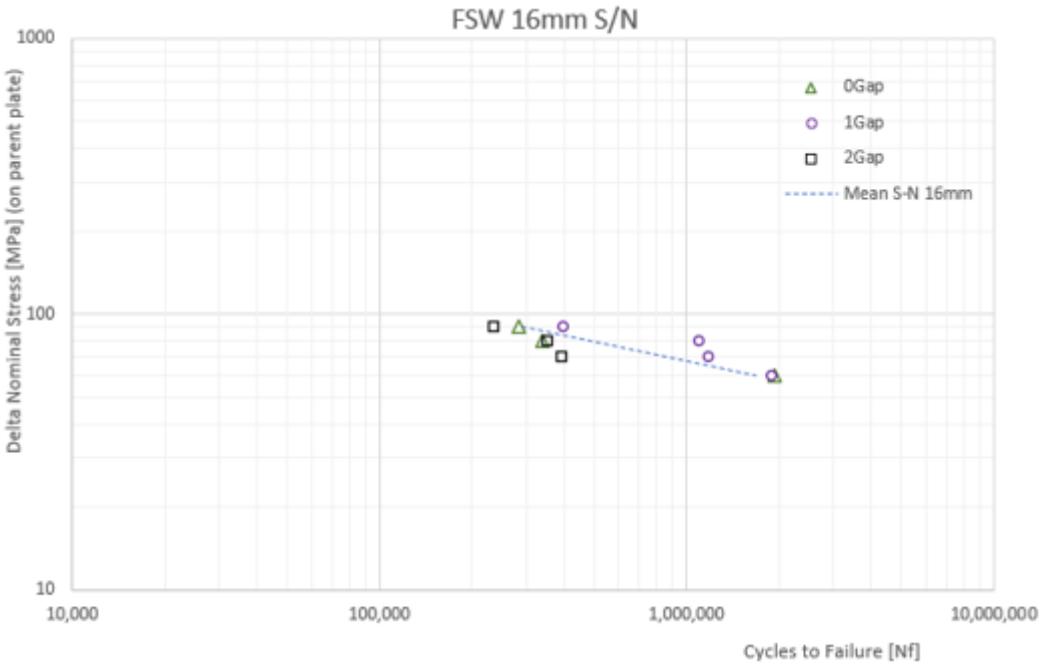

Figure 35: S-N curve of 16mm specimens.

5.4.2 22mm

Figure 36 shows the fatigue tests results of the 22mm specimens. Overall, there is less scatter between the test series compared to the 16mm specimens. For the 22mm specimens, gaps of 2mm had higher values than Gap0, and 1Gap performed worse than the average.

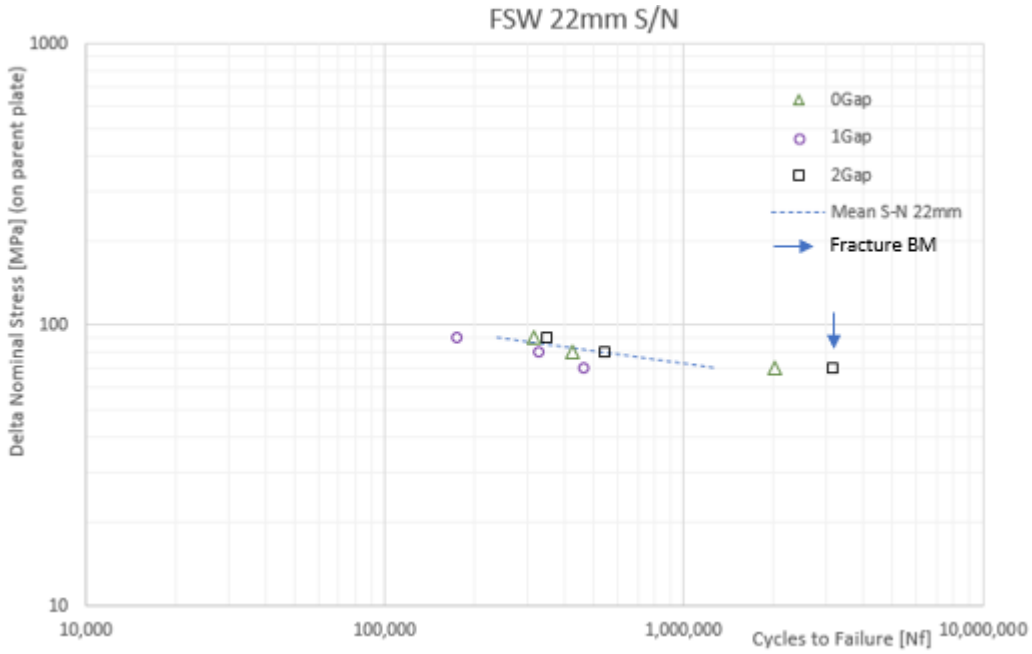

Figure 36: S-N curve of 22mm specimens.

5.5 Fracture examination

5.5.1 16 mm

After fatigue testing all specimens were visual inspected and pictured. Figure 37 shows macro fracture images of 16mm specimens after fatigue testing. All ten 16mm specimens had similar fractures with crack initiation from the unbonded region (red arrow) and crack propagation into the nugget stir zone. Figure 37(a) shows crack initiation from the bottom and residual fracture on top of weld (marked blue). It appears that the lower part of the fracture coincides with the profiles initial shape before welding, however from Figure 37(b) it is clear that there is complete bonding between the profiles. Marked in red in Figure 37(b) black dots are observed, this is believed to be caused by friction or by solvents used during CNC machining, as leaking of oil were observed during testing. Figure 38 shows an image of a specimen moments before fracture and during fatigue loading.

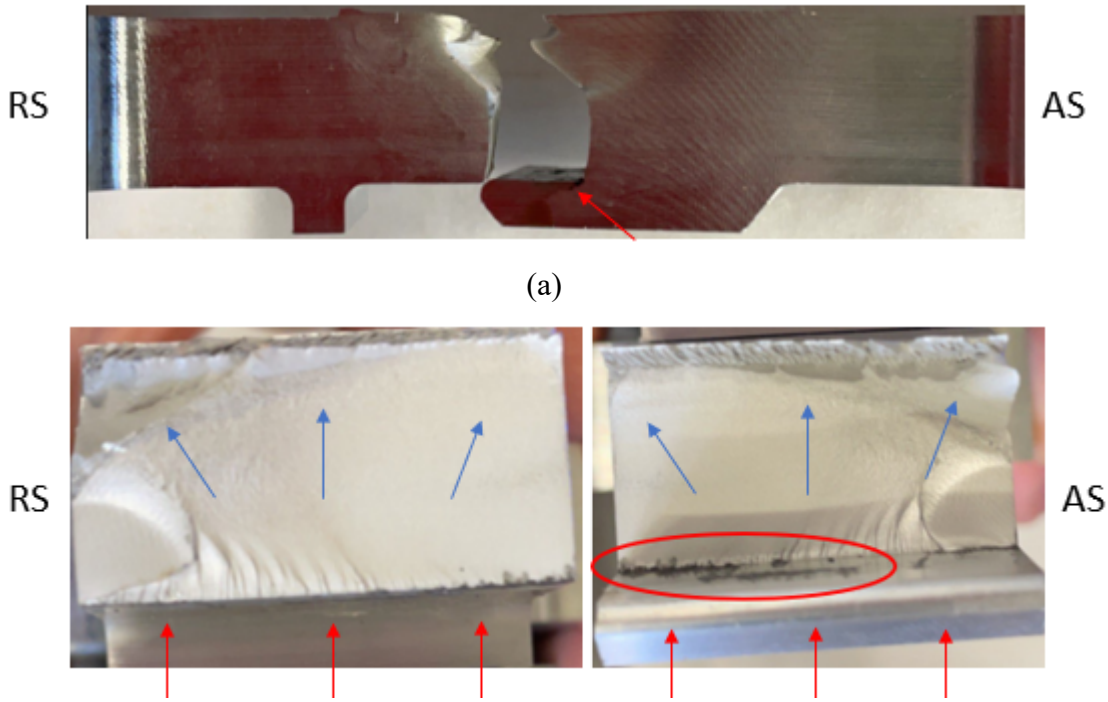

Figure 37: Macro fracture images of 16mm specimens after fatigue loading. Transverse image of fracture(a), crack initiation at the bottom (red arrow) and residual fracture (highlighted blue). Fracture of surface (b) shows crack initiation from the unbonded region (red arrow) with crack propagation (blue arrow). Black dots from solvents during CNC machining (highlighted red).

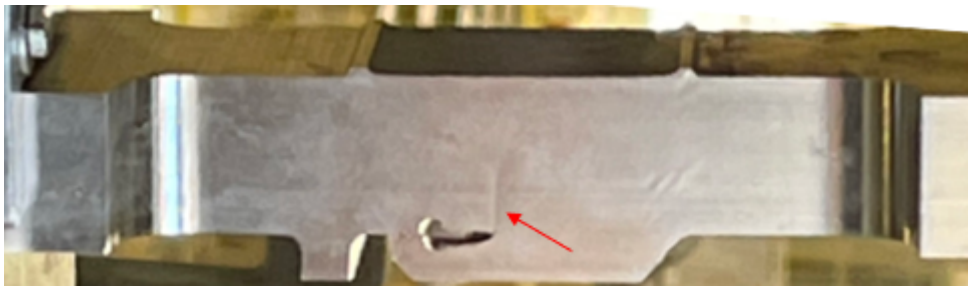

Figure 38: Image of 2Gap 16mm specimen under fatigue loading captured moments before fracture. Shows opening of the unbonded region and crack initiation at the bottom of the weld.

5.5.2 22 mm

Figure 39 show macro fracture images of 22mm specimens after fatigue testing. Eight out of nine 22mm specimens fractured in the HAZ. In contrast from 16mm specimens, the crack was initiated at the flashing from the top of the weld and propagated within the HAZ towards the unbound region (visual observation during testing).

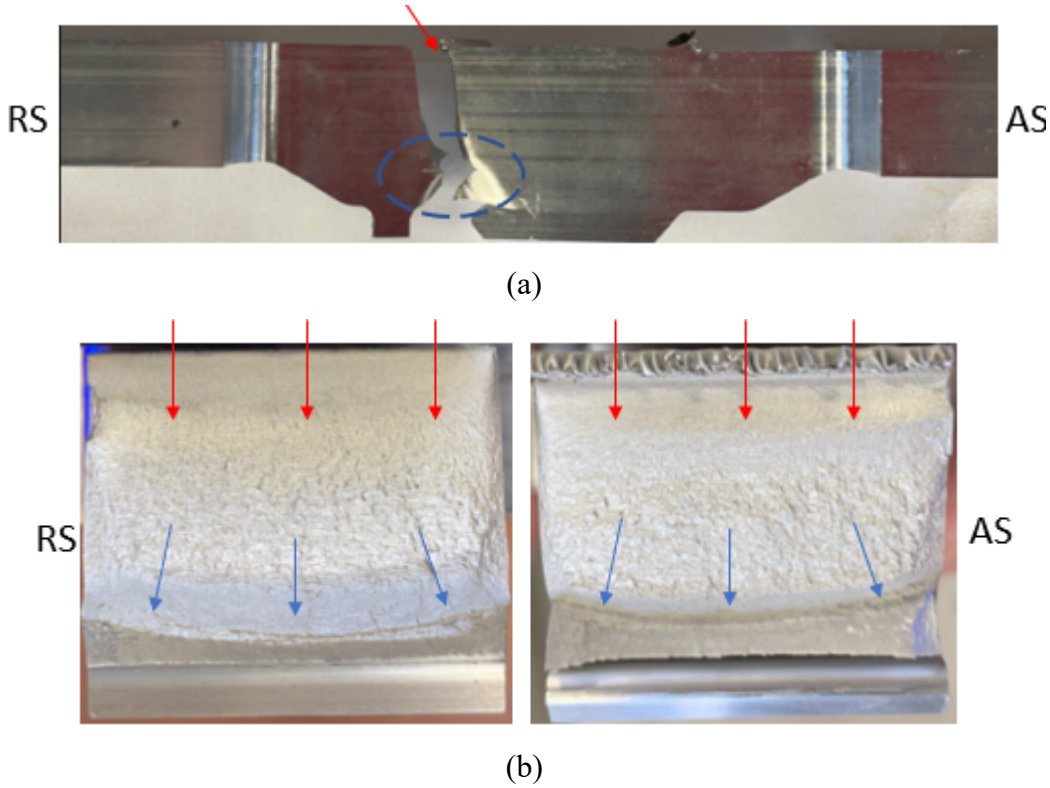

Figure 39: Macro fracture images of 22mm specimens after fatigue loading. Transverse image of fracture(a) crack initiation at the flashing at the top of weld (red arrow) and residual fracture (highlighted blue). Fracture of surface (b) shows that crack initiates from the flashing (red arrows) and crack propagation (blue arrow).

As mentioned, one tests shown in Figure 40 had a different fracture. This 2Gap 22mm specimen were tested at the lowest stress range and had the highest cycles to failure. From Figure 40(a) a large crack was observed during testing located in the NZ (red arrow), however fracture occurred in BM at the geometrical transition, as can be seen in Figure 40(b) (blue arrow). Origin of crack initiation and propagation in the nugget zone may be due to bonding defects even though this cannot be confirmed.

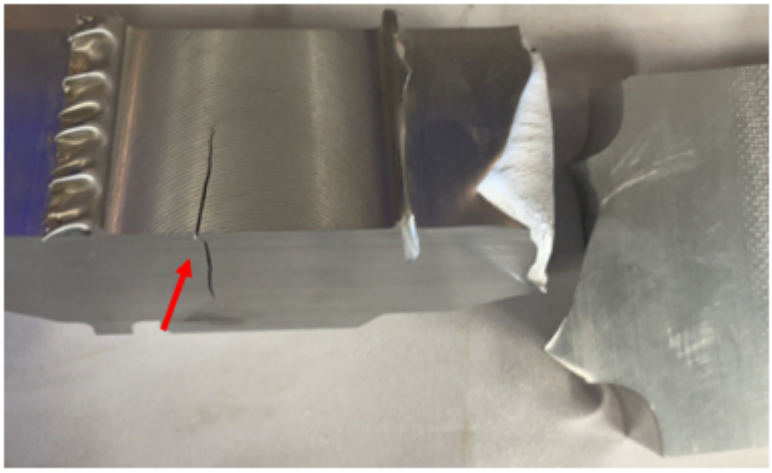

(a)

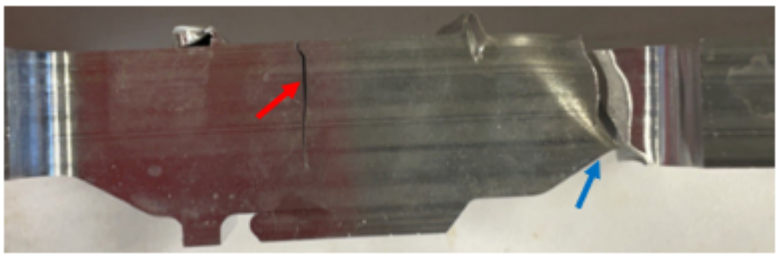

(b)

Figure 40: Macro fracture images of 22mm specimen after fatigue loading. Transverse image of fracture shows failure due to geometry (a), (b) shows the propagation of crack in the middle of the weld.

6. Discussion

6.1 Effect of specimen geometry

6.1.1 Deformation of tensile specimens during testing

As a starting point, the effect of specimen geometry on its deformation behaviour during testing should be examined. Figure 41 shows images of deformed 2Gap specimens of 16mm(a) and 22mm(b) at UTS, where red lines indicate the original shape and location prior to testing. From Figure 41(a) the specimens does not have any noticeable deformation under testing, as indicated by the red line. This was followed by the typical shear fracture in the HAZ, whereas the material is soft. In contrast, 22mm behaves slightly different. From Figure 41(b) the specimen bends out in an x-direction. The displacement causes tension forces to accumulate at the top of HAZ and at the geometrical transitions. This was followed by fracture in the geometrical transition with propagation towards the top of HAZ, as shown in the DIC strain analysis.

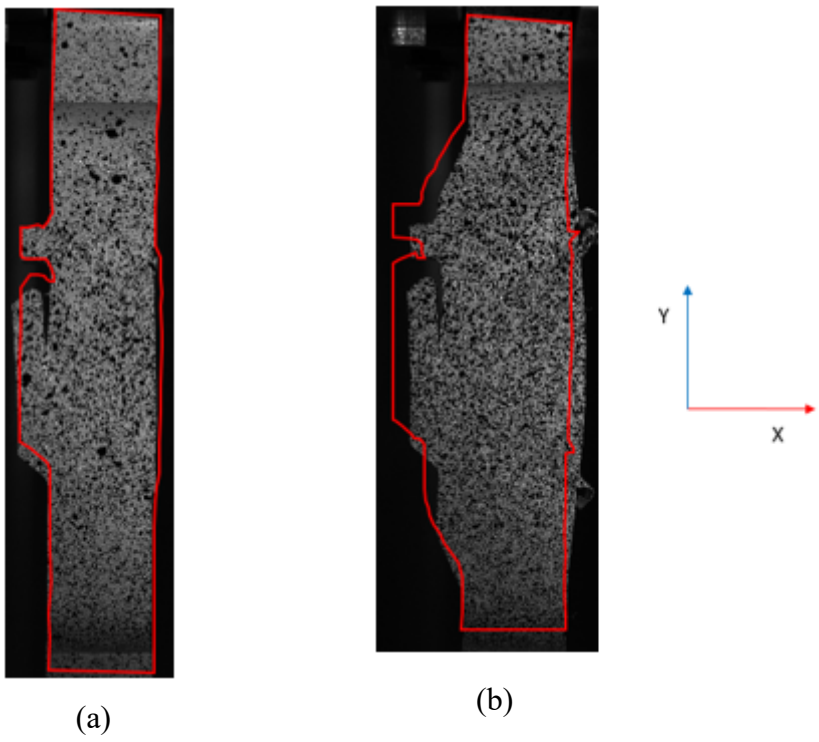

Figure 41:Images of deformed 2Gap specimens of 16mm(a) and 22mm(b) at UTS. Red lines indicate original shape and location prior to testing, y-axis is the loading direction.

The deformation behaviour of the 22mm specimens may have influenced the integrity of the specimen. With DIC post-analysis tools, the node displacement can be followed frame by frame and the starting point of deformation can be highlighted. Figure 42 shows the stress-strain curve of 22mm specimens at yield stess and maximum fatigue stress of $\Delta\sigma_{nom} = 90\ MPa$. Before yield stress, early deformation of 0.5mm in the x-direction is observed at top of HAZ. This deformation corelates well with the strain consentration at HAZ from the DIC analysis. In general, the tensile strength of the two joints had no significant difference between the different geometries and gaps, and the effect of deformation on the tensile properties appears to be limited.

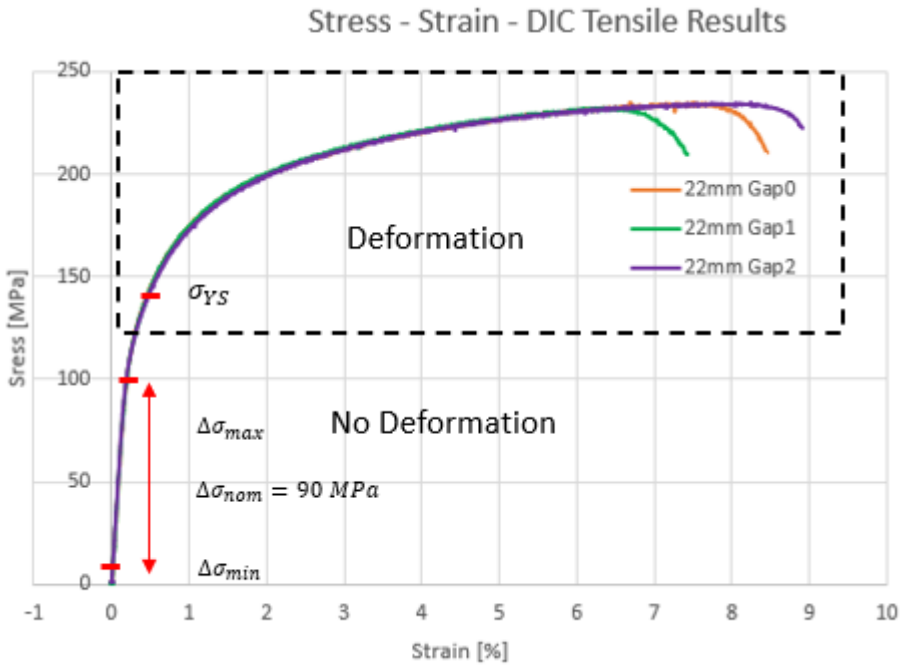

Figure 42: Stress-strain curve of 22mm specimens at yield stress and fatigue stress. Start of deformation is highlighted by dashed lines.

6.1.2 Deformation behaviour of 22mm during fatigue testing

When looking at maximum fatigue stress there was no noicable deformation. However, small amounts of strain localisation can be identified for the 22mm specimens, as shown in Figure 43, wheras total ε_{p1} of 0.10 at maximum fatigue stress. There was no noticble strain locatiation for the 16mm specimens at fatigue stress.

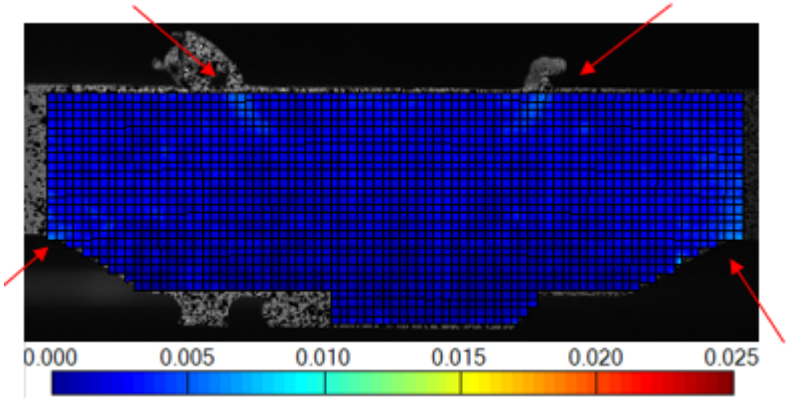

Figure 43: DIC image of 2Gap 22mm specimen at maximum fatigue stress $\Delta\sigma_{nom} = 90\ MPa$. Strain concentrations are highlighted with red arrows.

Regarding the influence of specimen geometry on fatigue behaviour, the findings indicate that in the case of the 16mm specimens, cracks tend to initiate at the unbonded region located at the weld root. For the 22mm specimens, cracks tend to initiate at the flashing on the top of the weld and propagated within the HAZ towards the unbounded region. Local geometry of welds, such as sharp transitions, and different bonding defects, cause local stress concentrations at the joint. These defects are commonly associated as the starting point of fatigue cracks [47], as fatigue is more sensitive to stress concentrations [48]. When testing up to $3 \cdot 10^6$ cycles, one 22mm specimen fractured in the BM, which suggests that the profile geometry may have an influence high-cycle fatigue life. If testing had continued at even higher N_f, it is believed that effect of geometry on the 22mm specimens would have been more pronounced. As results from previous testing campaigns carried out by the partners in Alubridge, observed that fracture occurred in the BM at high cycles. This, with addition to run-out tests at high cycles, few tests were carried out on the 22mm specimens in the Alubridge project.

6.2 Effect of gap tolerances on fatigue properties

6.2.1 Comparison of fatigue results against Alubridge data

Figure 44 shows the fatigue test results of 16mm specimens compared to those obtained in the Alubridge project for comparable specimens (without artificial gaps, FSW 16mm marked red). Similar results for the 22mm specimens are shown in Figure 45.

As can be seen from Figure 44, data obtained from the present work, behaves in a similar manner of those previously obtained in the Alubridge project. Even tough, there are some scatter in the data based on the different gap tolerances. The variation seems to be within the scatter of Alubridge data, this in the present case, the applied gap seems to have little effect on the overall fatigue behaviour.

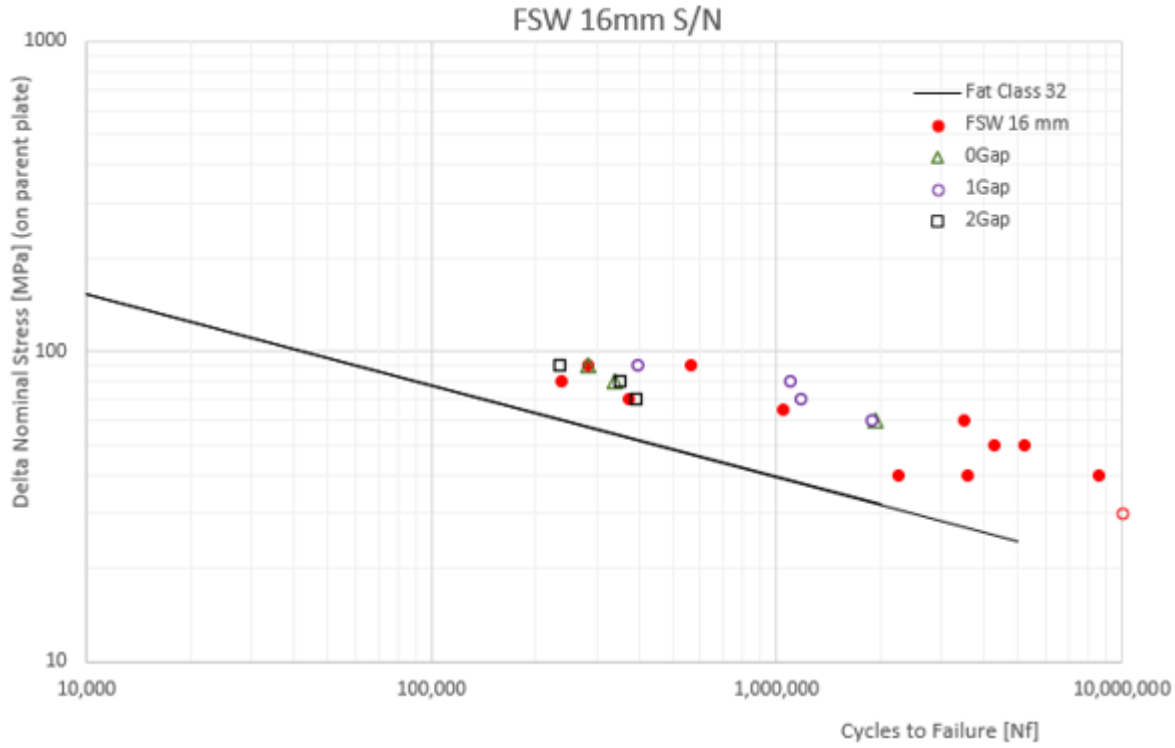

Figure 44: Fatigue results with previous Alubridge results of 16mm specimens.

As can be seen from the Figure 45, the general results are similar to the 16mm specimens, again the data falls in line with Alubridge data and in fact spread in data appears to be slightly lower. However, the amount of specimens tested in the Alubridge project is fairly low. In both cases 16mm and 22mm specimen fatigue test results lies above the Eurocode design class for comparable welded joints. And the applied gap seems to have little effect on the fatigue properties.

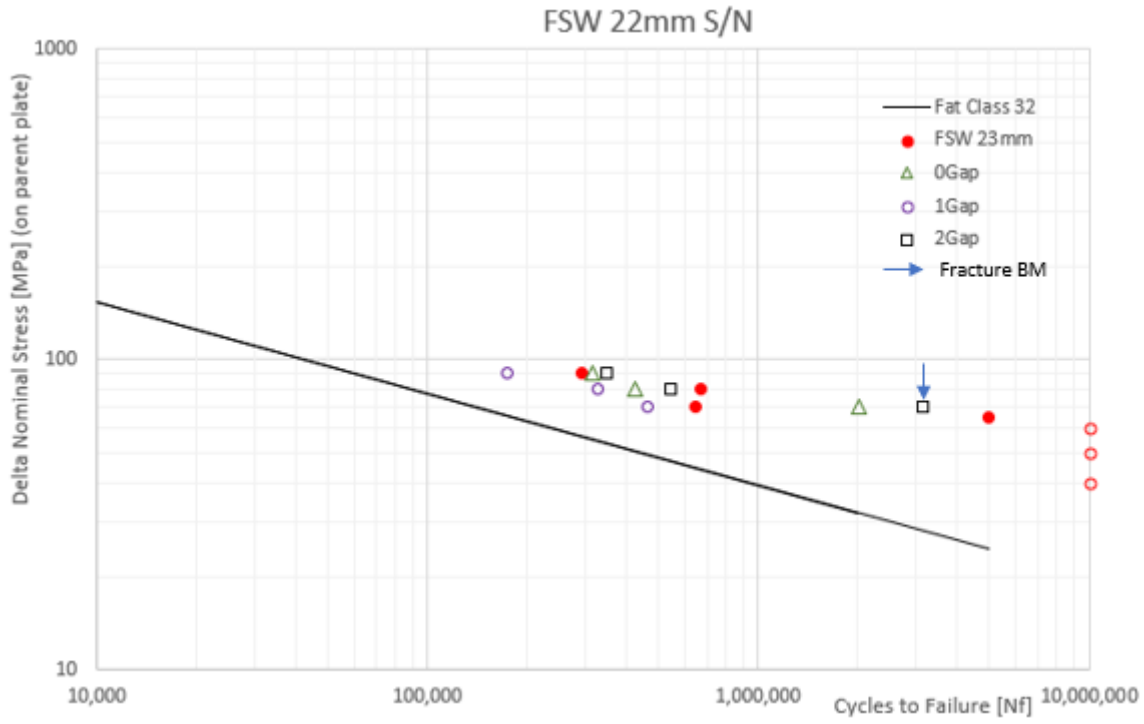

Figure 45:Fatigue results with previous Alubridge results of 22mm specimens.

6.3 Evaluation of the fatigue test results bases on fracture location

From the fracture examination (section 5.5), most of 22mm specimens fractured along the HAZ along the weld thickness of 22mm. However, the previously shown S-N curves ref figure 44, and 45. Are based on nominal cross area of $(16 \cdot 30)mm^2$ as done previously in the Alubridge project. By taking to account for the fracture location the actual cross area becomes larger. This is why in the Figure 46; the fatigue test has been adjusted for actual cross section area of $(22 \cdot 30)mm^2$.

As a result, the data drops relatively low and falls on top of the design curve from Eurocode 9, which is based on 97,5% probability of no failure [32], [61]. Questions should be asked if it was correct to use the nominal cross area of $(16 \cdot 30)mm^2$, when eighth out of nine fractures occurred in the weld cross section area of $(22 \cdot 30)mm^2$ for the 22mm specimens. At high cycles, only one of the specimens fractured in the BM of $(16 \cdot 30)mm^2$. This should be further evaluated as the fatigue properties drop by a considerable amount.

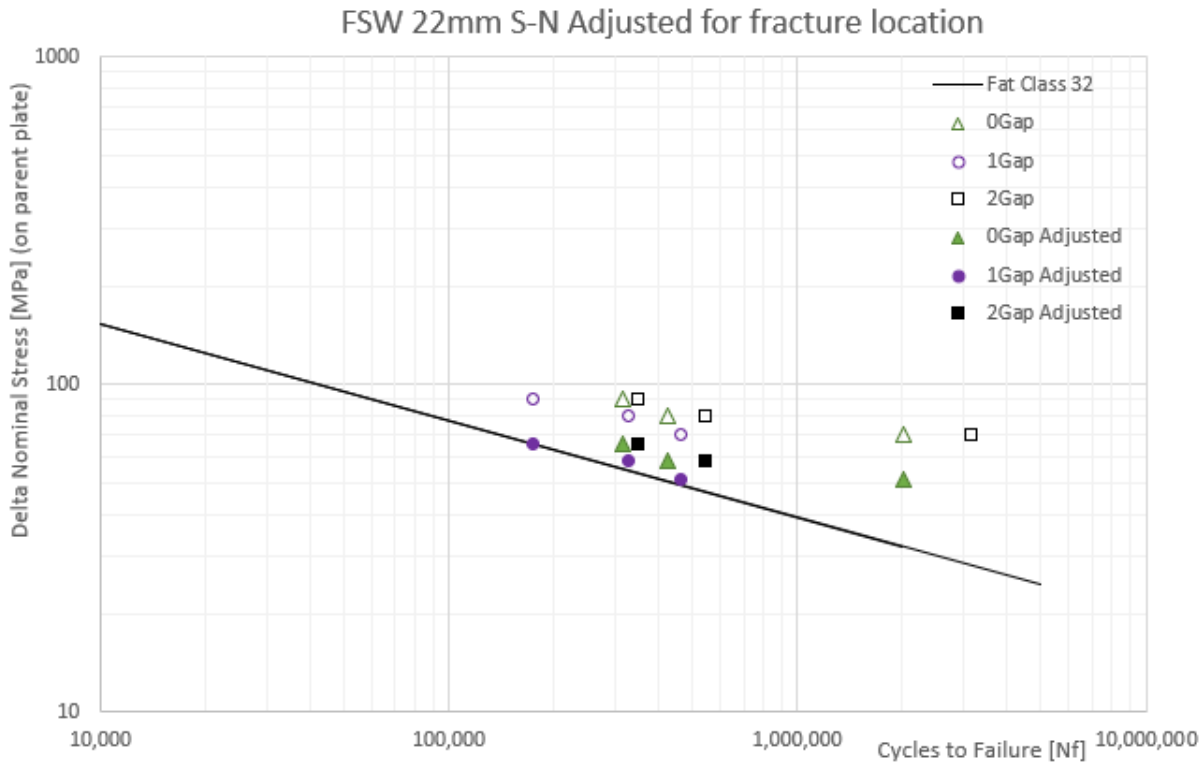

Figure 46: Fatigue results after accounting for fracture locations of the 22mm specimens.

6.4 Gap consistency

Gap tolerances had no obvious effect on tensile results and the fatigue life. However, one should question the actual effective gaps achieved after welding of the two joints. R. Rolle reported that it was difficult to achieve a consistent gap between the profiles, as gaps in the centre started to deviate from gaps at the edges [5]. Shrinking of centre gap was observed as the FSW-tool moved along the joint line, with gaps increasing at the edges. Due to this phenomenon, it is uncertain how large the actual resulting gaps were. However, in an industrial setting if the measured maximum gap along weld line over the entire profile does not exceed 2mm. The indication is that it's possible should produce sound FS welds at this gap.

Several researcher have performed studies on mating variations and their effect on joint strength in FSW [28], [29]. Among the common mating variations which is shown in Figure 47, the most common and difficult to predict is the gap between abutted plates or profiles [29]. The present work does not consider the high difference, Figure 47(b) which may occur due to twisting of profiles after extrusion, or the misalignment Figure 47(c) with the FS-tool due to straightness errors along the profile and how this effect the joint quality. The topic of mating variations is rather complex as it is affected by the aluminium extrusion process (as it affects the resulting profile tolerances), and the FSW process (such as applied welding parameters and clamping conditions) which affects the weld quality.

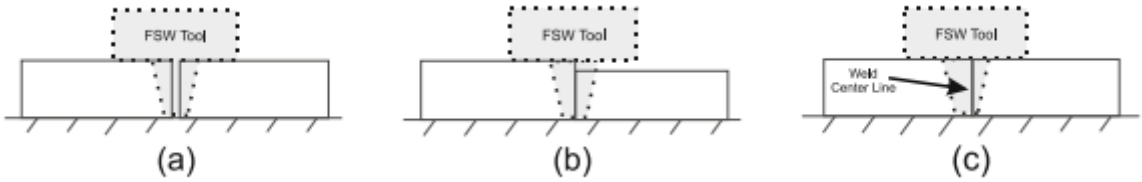

Figure 47: Most common mating variations in FSW, Gap (a), mismatch (b), misalignment (c) [29].

More research is needed regarding the effect of as-extruded profile tolerances on the mechanical properties of these joints. The FS welds in the present work has been fabricated under optimal laboratory conditions, with relatively short 1 meters long profiles. In an industrial setting, the profiles would have been much longer, up to 12 meters whereas profile variances would be larger [1].

7. Conclusion

In the present work for the Alubridge project, investigation of the effect of profile geometry and gap tolerances on the mechanical response of thick section (16mm and 22mm) AA6082-T6 FS Welds, have been experimented and examined through fatigue and tensile testing, including DIC analysis and fatigue testing of specimens with different gaps of (0, 1, 2) mm. The main conclusions can be summarised as follows:

- In general, the tensile strength of the two different geometries (16mm and 22mm) have an UTS of 242 MPa and 234 MPA respectively. These results indicate that there was no significant difference in tensile properties of the different geometries and gaps.
- Effect of geometry on the deformation behaviour during tensile testing had little effect on 16mm specimens. For the 22mm specimens, deformation was observed before yield stress. However, its effect on tensile properties appears to be limited.
- No deformation were present at fatigue stress. However, small amounts of strain localisation can be identified for the 22mm specimens at fatiuge stress, this was not the case for 16mm specimens.
- Based on the same experimental setup as done previously by partners in the Alubridge project, gap tolerances had no obvious effect on the fatigue life. The fatigue data obtained from the present work, behaves in a similar manner of those previously obtained in the Alubridge project.
- When evaluating the fatigue results for the fracture location the actual cross area becomes larger. Questions should be asked if it was correct to use the nominal cross area of $(16 \cdot 30)mm^2$, when eighth out of nine fractures occurred in the weld cross section area of $(22 \cdot 30)mm^2$ for the 22mm specimens. At high cycles, only one of the specimens fractured in the BM of $(16 \cdot 30)mm^2$. This should be further evaluated as the fatigue properties drop by a considerable amount.
- One should question the actual effective gaps achieved after welding of the two joints. As it has been reported by R. Rolle, it was difficult to achieve a consistent gap between the profiles, and it is uncertain how large the actual resulting gaps were. In an industrial setting if the measured maximum gap along weld line over the entire profile does not exceed 2mm. The indication is that it's possible should produce sound FS welds at this gap. However, there are a variety of suggested further work.

Suggested future work

It is uncertain how accurate gap tolerances it is possible to achieve, or what type of challenges that can occur due to other geometrical tolerances, such as twist, bow and straightness tolerances and the effect of deformation in different directions on the intended 12-meter-long profiles. Even though this is not part of this work, the tool design may be improved to enable FSW for larger gaps.

References

[1] A. Djedid, M. Guillot, V. Desjardins, C.-D. Annan, and M. Fafard, 'Design and Fabrication of Bridge Decks made from Extruded Aluminium', **軽金属溶接**, vol. 58, no. Supplement, pp. 138s–144s, 2020, doi: 10.11283/jlwa.58.138s.

[2] F. M. Mazzolani, *Aluminium Structural Design*. Springer, 2014.

[3] R. P. Verma and M. Kumar Lila, 'A short review on aluminium alloys and welding in structural applications', *Mater. Today Proc.*, vol. 46, pp. 10687–10691, Jan. 2021, doi: 10.1016/j.matpr.2021.01.447.

[4] J. K. Paik, S. van der Veen, A. Duran, and M. Collette, 'Ultimate compressive strength design methods of aluminum welded stiffened panel structures for aerospace, marine and land-based applications: A benchmark study', *Thin-Walled Struct.*, vol. 43, no. 10, pp. 1550–1566, Oct. 2005, doi: 10.1016/j.tws.2005.06.003.

[5] R. Rolle, 'Gap Tolerance for Friction Stir Welding of Large, Extruded Aluminum Profiles', Master thesis, NTNU, 2022. Accessed: Dec. 06, 2022. [Online]. Available: https://ntnuopen.ntnu.no/ntnu-xmlui/handle/11250/3024752

[6] 'Davis. Aluminum and Aluminum Alloys'. Accessed: Oct. 31, 2022. [Online]. Available: https://materialsdata.nist.gov/bitstream/handle/11115/173/Aluminum%20and%20Aluminum%20Alloys%20Davis.pdf?sequence=3&isAllowed=y

[7] J. G. Kaufman, *Introduction to Aluminum Alloys and Tempers*. ASM International, 2000.

[8] M. Abbass and H. Abed, *Behavior of Different Welded Joints in Erosive-Corrosive Media*. 2014.

[9] J. V. Jakobsen, 'Microstructure and Mechanical Properties of Welded AA6082 Aluminium Alloys', Master thesis, NTNU, 2016. Accessed: May 10, 2023. [Online]. Available: https://ntnuopen.ntnu.no/ntnu-xmlui/handle/11250/2406949

[10] 'Aluminum alloys: selection and application', *Aluminium Guide*, May 31, 2017. https://aluminium-guide.com/aluminievye-splavy-klassifikacija-primenenie-svojistva-kharakteristik/ (accessed Mar. 20, 2023).

[11] P. Mukhopadhyay, ‘Alloy Designation, Processing, and Use of AA6XXX Series Aluminium Alloys’, *ISRN Metall.*, vol. 2012, pp. 1–15, Apr. 2012, doi: 10.5402/2012/165082.

[12] J. E. Hatch, *Aluminum: Properties and Physical Metallurgy*. ASM International, 1984.

[13] C. Hsu, K. O’Reilly, B. Cantor, and R. Hamerton, ‘Non-equilibrium reactions in 6xxx series Al alloys’, *Mater. Sci. Eng. -Struct. Mater. Prop. Microstruct. Process. - MATER SCI ENG -STRUCT MATER*, vol. 304, pp. 119–124, May 2001, doi: 10.1016/S0921-5093(00)01467-2.

[14] S. Karabay, M. Zeren, and M. Yilmaz, ‘Investigation extrusion ratio effect on mechanical behaviour of extruded alloy AA-6063’, *J. Mater. Process. Technol.*, vol. 135, pp. 101–108, Apr. 2003, doi: 10.1016/S0924-0136(02)01110-X.

[15] L. Ding, Z. Jia, Z. Zhang, R. E. Sanders, Q. Liu, and G. Yang, ‘The natural aging and precipitation hardening behaviour of Al-Mg-Si-Cu alloys with different Mg/Si ratios and Cu additions’, *Mater. Sci. Eng. A*, vol. 627, pp. 119–126, Mar. 2015, doi: 10.1016/j.msea.2014.12.086.

[16] ‘O. Reiso, Extrusion of AlMgSi Alloys’, *kipdf.com*. https://kipdf.com/extrusion-of-almgsi-alloys_5aad885a1723ddf63b970cf6.html (accessed Oct. 24, 2022).

[17] ‘DIETER, George Ellwood; BACON, David. Mechanical metallurgy. New York: McGraw-hill, 1976.’

[18] O. R. Myhr, Ø. Grong, and K. O. Pedersen, ‘A Combined Precipitation, Yield Strength, and Work Hardening Model for Al-Mg-Si Alloys’, *Metall. Mater. Trans. A*, vol. 41, no. 9, pp. 2276–2289, Sep. 2010, doi: 10.1007/s11661-010-0258-7.

[19] A. Simar, Y. Bréchet, B. de Meester, A. Denquin, C. Gallais, and T. Pardoen, ‘Integrated modeling of friction stir welding of 6xxx series Al alloys: Process, microstructure and properties’, *Prog. Mater. Sci.*, vol. 57, no. 1, pp. 95–183, Jan. 2012, doi: 10.1016/j.pmatsci.2011.05.003.

[20] O. Grong, ‘Recent Advances in Solid-State Joining Of Aluminum’, *Weld. J.*, vol. 91, pp. 26–33, Jan. 2012.

[21] S. K. Fjeldbo, Y. Li, K. Marthinsen, and T. Furu, ‘Through-process sensitivity analysis on the effect of process variables on strength in extruded Al–Mg–Si alloys’, *J. Mater. Process. Technol.*, vol. 212, no. 1, pp. 171–180, Jan. 2012, doi: 10.1016/j.jmatprotec.2011.08.020.

[22] S. Zajac, B. Bengtsson, and C. Jönsson, ‘Influence of Cooling after Homogenisation and Reheating to Extrusion on Extrudability and Final Properties of AA 6063 and AA6082 Alloys’, *Mater. Sci. Forum - MATER SCI FORUM*, vol. 396, pp. 399–404, Jul. 2002, doi: 10.4028/www.scientific.net/MSF.396-402.399.

[23] ‘Anodizing | Aluminum Extruders Council’. https://aec.org/anodizing (accessed Dec. 04, 2022).

[24] B. Milkereit, M. Starink, P. A. Rometsch, C. Schick, and O. Kessler, ‘Review of the Quench Sensitivity of Aluminium Alloys: Analysis of the Kinetics and Nature of Quench-Induced Precipitation’, *Materials*, vol. 12, p. 4083, Dec. 2019, doi: 10.3390/ma12244083.

[25] O. S. Es-Said *et al.*, 'Warpage Behavior of 7075 Aluminum Alloy Extrusions', *J. Mater. Eng. Perform.*, vol. 16, no. 2, pp. 242–247, Apr. 2007, doi: 10.1007/s11665-007-9044-0.

[26] K. Strobel, M. A. Easton, L. Sweet, M. J. Couper, and J.-F. Nie, 'Relating Quench Sensitivity to Microstructure in 6000 Series Aluminium Alloys', *Mater. Trans.*, vol. 52, no. 5, pp. 914–919, 2011, doi: 10.2320/matertrans.L-MZ201111.

[27] T. Zappia, '7 - Inspection and quality control in friction stir welding', in *Friction Stir Welding*, D. Lohwasser and Z. Chen, Eds., in Woodhead Publishing Series in Welding and Other Joining Technologies. Woodhead Publishing, 2010, pp. 183–212. doi: 10.1533/9781845697716.1.183.

[28] H. Ma 'Gap-tolerance control for friction stir butt welding of 2A14 aluminium alloy | Elsevier Enhanced Reader'. https://reader.elsevier.com/reader/sd/pii/S0263224119307729?token=72DFF595C87DBC283718A17F5D91DCC98209DEAC089993E1EE8EED4CDA1E2E6165F324501269BF9D46C340C5F45ADD82&originRegion=eu-west-1&originCreation=20230329131226 (accessed Mar. 29, 2023).

[29] E. G. Cole *et al.*, 'Stability of the friction stir welding process in presence of workpiece mating variations', *Int. J. Adv. Manuf. Technol.*, vol. 63, no. 5, pp. 583–593, Nov. 2012, doi: 10.1007/s00170-012-3946-1.

[30] O. R. Myhr, Ø. Grong, H. G. Fjær, and C. D. Marioara, 'Modelling of the microstructure and strength evolution in Al–Mg–Si alloys during multistage thermal processing', *Acta Mater.*, vol. 52, no. 17, pp. 4997–5008, Oct. 2004, doi: 10.1016/j.actamat.2004.07.002.

[31] Z. Liang, X. Wang, C. Cai, and D. Wang, 'Microstructure and Mechanical Properties of Thick Plate Friction Stir Welds for 6082-T6 Aluminum Alloy', *High Temp. Mater. Process.*, vol. 38, no. 2019, pp. 525–532, Jan. 2019, doi: 10.1515/htmp-2018-0074.

[32] 'Eurokode9'. https://www.standard.no/no/nettbutikk/produktkatalogen/produktpresentasjon/?ProductID=424301 (accessed Dec. 05, 2022).

[33] K. Wayne Stephan |. Nicholas, David |. Thomas, 'Friction Stir Welding: Invention, Innovation and Application'. https://www.twi-global.com/technical-knowledge/published-papers/friction-stir-welding-invention-innovations-and-applications-march-2001.aspx (accessed Oct. 20, 2022).

[34] Z. Y. Ma, A. H. Feng, D. L. Chen, and J. Shen, 'Recent Advances in Friction Stir Welding/Processing of Aluminum Alloys: Microstructural Evolution and Mechanical Properties', *Crit. Rev. Solid State Mater. Sci.*, vol. 43, no. 4, pp. 269–333, Jul. 2018, doi: 10.1080/10408436.2017.1358145.

[35] Y. Yang *et al.*, 'Research progress on the microstructure and mechanical properties of friction stir welded AlLi alloy joints', *J. Manuf. Process.*, vol. 82, pp. 230–244, Oct. 2022, doi: 10.1016/j.jmapro.2022.07.067.

[36] W. M. Thomas and E. D. Nicholas, 'Friction stir welding for the transportation industries', *Mater. Des.*, vol. 18, no. 4, pp. 269–273, Dec. 1997, doi: 10.1016/S0261-3069(97)00062-9.

[37] P. L. Threadgill, A. J. Leonard, H. R. Shercliff, and P. J. Withers, ‘Friction stir welding of aluminium alloys’, *Int. Mater. Rev.*, vol. 54, no. 2, p. 46, 2009.

[38] R. Nandan, T. DebRoy, and H. K. D. H. Bhadeshia, ‘Recent advances in friction-stir welding – Process, weldment structure and properties’, *Prog. Mater. Sci.*, vol. 53, no. 6, pp. 980–1023, Aug. 2008, doi: 10.1016/j.pmatsci.2008.05.001.

[39] ‘hydro-friction-stir-welding.pdf’. Accessed: Apr. 25, 2023. [Online]. Available: https://www.hydro.com/globalassets/download-center/publications/hydro-friction-stir-welding.pdf

[40] R. S. Mishra and Z. Y. Ma, ‘Friction stir welding and processing’, *Mater. Sci. Eng. R Rep.*, vol. 50, no. 1, pp. 1–78, Aug. 2005, doi: 10.1016/j.mser.2005.07.001.

[41] ‘T.Khaled, AN OUTSIDER LOOKS AT FRICTION STIR WELDING’. Accessed: Dec. 04, 2022. [Online]. Available: https://citeseerx.ist.psu.edu/document?repid=rep1&type=pdf&doi=8dd24416352832b341fbc9c6c4a86091ff9db5cf

[42] P. M. G. P. Moreira, A. M. P. de Jesus, A. S. Ribeiro, and P. M. S. T. de Castro, ‘Fatigue crack growth in friction stir welds of 6082-T6 and 6061-T6 aluminium alloys: A comparison’, *Theor. Appl. Fract. Mech.*, vol. 50, no. 2, pp. 81–91, Oct. 2008, doi: 10.1016/j.tafmec.2008.07.007.

[43] C. Gallais *et al.*, ‘Multiscale Analysis of the Strength and Ductility of AA 6056 Aluminum Friction Stir Welds’, *Metall. Mater. Trans. A*, vol. 38, no. 5, pp. 964–981, May 2007, doi: 10.1007/s11661-007-9121-x.

[44] C. R. Breivik, ‘Mechanical Properties of Gas Metal Arc and Friction Stir AA6082-T6 Weldments’, Master thesis, Institutt for materialteknologi, 2013. Accessed: Dec. 05, 2022. [Online]. Available: https://ntnuopen.ntnu.no/ntnu-xmlui/handle/11250/249324

[45] D. Texier, "Fatigue performances of FSW and GMAW aluminum alloys welded joints_ Competition between microstructural and structural-contact-fretting crack initiation"| Elsevier Enhanced Reader’. https://reader.elsevier.com/reader/sd/pii/S0142112318302469?token=5AF2711EAC6EC59FE6B997D37555113321C501FDEAAF5AE7F6CCDC47117599EF002A74BA8CF66609218AE8B56B2563BD&originRegion=eu-west-1&originCreation=20221019073847 (accessed Oct. 20, 2022).

[46] G. Çam and S. Mistikoglu, ‘Recent Developments in Friction Stir Welding of Al-alloys’, *J. Mater. Eng. Perform.*, vol. 23, no. 6, pp. 1936–1953, Jun. 2014, doi: 10.1007/s11665-014-0968-x.

[47] A. F. Liu, *Mechanics and Mechanisms of Fracture: An Introduction*. ASM International, 2005.

[48] A. Almar-Næss, *Fatigue handbook: offshore steel structures*. Trondheim: Tapir, 1985. Accessed: Oct. 10, 2022. [Online]. Available: https://urn.nb.no/URN:NBN:no-nb_digibok_2016062708038

[49] A. Chaudhary, R. Mishra, M. Anwar Ali Anshari, M. Imam, and V. Chintapenta, 'Experimental and numerical investigation of laser-FSW hybrid welding technique for high strength materials', *2022 Int. Conf. Mater. Sustain. Manuf. Technol.*, vol. 65, pp. 3437–3448, Jan. 2022, doi: 10.1016/j.matpr.2022.05.579.

[50] T. Wayne, 'Friction Stir Welding and Related Process Characteristics'. https://www.twi-global.com/technical-knowledge/published-papers/friction-stir-welding-and-related-friction-process-characteristics-april-1998.aspx (accessed Oct. 20, 2022).

[51] P. M Jonathan |. Martin, Jonathan |. Threadgill, Philip |. Ahmed, 'Friction Stir Welding of Thick Section Aluminium Alloys'. https://www.twi-global.com/technical-knowledge/published-papers/recent-developments-in-friction-stir-welding-of-thick-section-aluminium-alloys-march-2007.aspx (accessed Oct. 20, 2022).

[52] A. Silva-Magalhães, J. De Backer, J. Martin, and G. Bolmsjö, 'In-situ temperature measurement in friction stir welding of thick section aluminium alloys', *J. Manuf. Process.*, vol. 39, pp. 12–17, Mar. 2019, doi: 10.1016/j.jmapro.2019.02.001.

[53] A. S. Hamada *et al.*, 'The microstructural evolution of friction stir welded AA6082-T6 aluminum alloy during cyclic deformation', *Mater. Sci. Eng. A*, vol. 642, pp. 366–376, Aug. 2015, doi: 10.1016/j.msea.2015.06.100.

[54] P. Upadhyay and A. Reynolds, 'Effect of Backing Plate Thermal Property on Friction Stir Welding of 25-mm-Thick AA6061', *Metall. Mater. Trans. A*, vol. 45, no. 4, pp. 2091–2100, Apr. 2014, doi: 10.1007/s11661-013-2121-0.

[55] 'Dr.techn. olav olsen AS,langenuen suspension bridge aluminium girder alternative'. Accessed: Dec. 03, 2022. [Online]. Available: https://www.hydro.com/contentassets/be6d51d284cb4ea39a67a4e0cefd23fa/langenuen-suspension-bridge-aluminium-girder-alternative.pdf

[56] 'AluBridge – Robust design and efficient production of durable and sustainable aluminium bridges', *SINTEF*, Jun. 22, 2021. https://www.sintef.no/en/projects/2020/alubridge-robust-design-and-efficient-production-of-durable-and-sustainable-aluminium-bridges/ (accessed Jun. 22, 2023).

[57] N. McCormick and J. Lord, 'Digital Image Correlation', *Mater. Today*, vol. 13, no. 12, pp. 52–54, Dec. 2010, doi: 10.1016/S1369-7021(10)70235-2.

[58] E. Fagerholt 'Measuring discontinuous displacement fields in cracked specimens using digital image correlation with mesh adaptation and crack-path optimization | Elsevier Enhanced Reader'. https://reader.elsevier.com/reader/sd/pii/S0143816612002801?token=D981407A6332C0F2CB3142B3020274BEEBEC306006E1BDA9F4D9B02AF81F2901E78A9AC63717DF234D8C47AAC4AE3DDF&originRegion=eu-west-1&originCreation=20230503145246 (accessed May 03, 2023).

[59] B. Pan, 'Digital image correlation for surface deformation measurement: historical developments, recent advances and future goals', *Meas. Sci. Technol.*, vol. 29, no. 8, p. 082001, Jun. 2018, doi: 10.1088/1361-6501/aac55b.

[60] ‘ASTM E739:10(2015)’. https://handle.standard.no/no/Nettbutikk/produktkatalogen/Produktpresentasjon/?ProductID=785160 (accessed Jun. 12, 2023).

[61] J. Carol, ‘Statistical analysis of fatigue test data’. https://www.twi-global.com/technical-knowledge/published-papers/statistical-analysis-of-fatigue-test-data.aspx (accessed May 11, 2023).

9.1 Appendix

APENDIX A

Detailed drawing with dimensions of the 16mm specimens, 22mm specimens has the same general geometry.

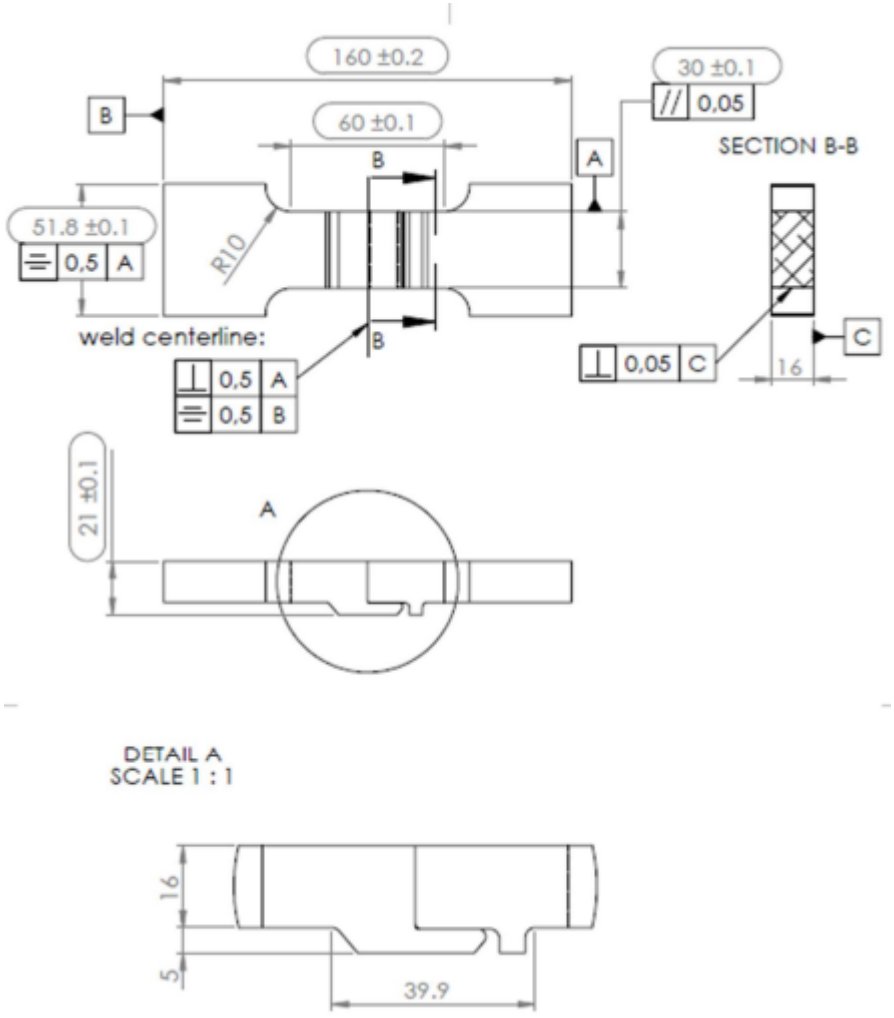

APENDIX B

Fatigue test tables

		16mm specimens			
Nr/stress	thickness	width	Fmin	Fmax	Nf
-	[mm]	[mm]	[N]	[N]	Cycles
0gap90	16	30	4800	48000	283013
0gap80	16	30	4266.7	42667	338826
0gap60	16	30	3200	32000	1942825
1gap90	16	30	4800	48000	396283
1gap80	16	30	4266.7	42667	1089562
1gap70	16	30	3733.3	37333	1171137
1gap60	16	30	3200	32000	1879889
2gap90	16	30	4800	48000	235183
2gap80	16	30	4266.7	42667	352875
2gap70	16	30	3733.3	37333	389908

		22mm specimens			
Nr/Stress	thickness	width	Fmin	Fmax	Nf
-	[mm]	[mm]	[N]	[N]	Cycles
0gap90	16	30	4800	48000	313634
0gap80	16	30	4266.7	42667	421654
0gap70	16	30	3733.3	37333	2010415
1gap90	16	30	4800	48000	173842
1gap80	16	30	4266.7	42667	325215
1gap70	16	30	3733.3	37333	462876
2gap90	16	30	4800	48000	347542
2gap80	16	30	4266.7	42667	541507
2gap70	16	30	3733.3	37333	3155984

APPENDIX C

1. Yield Strength

0Gap

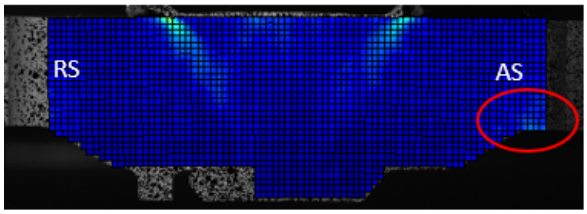

1Gap

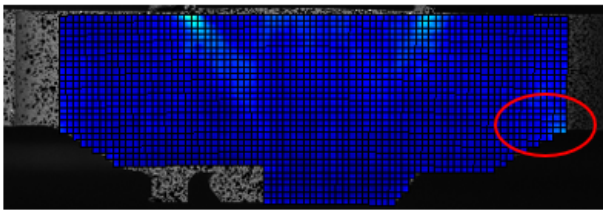

2Gap

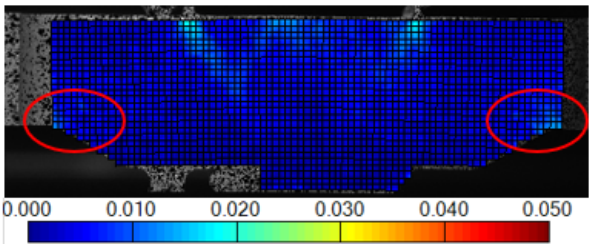

2.UTS

0Gap

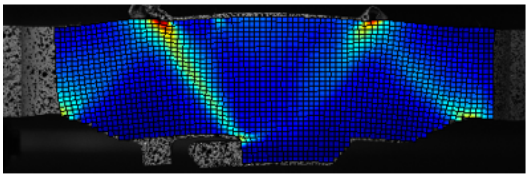

1Gap

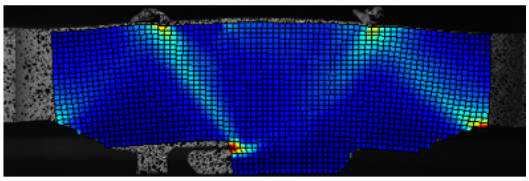

2Gap

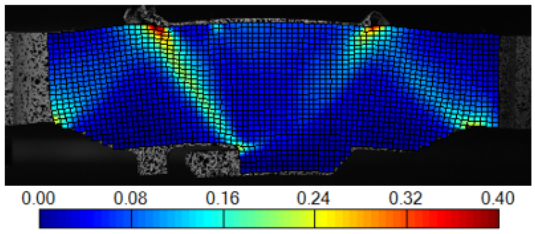

3. Strain at fracture

0Gap

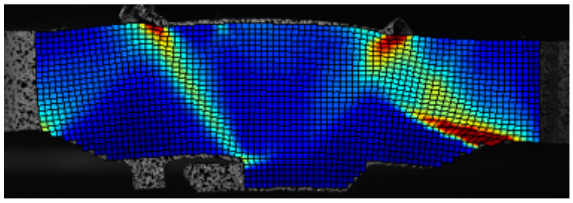

1Gap

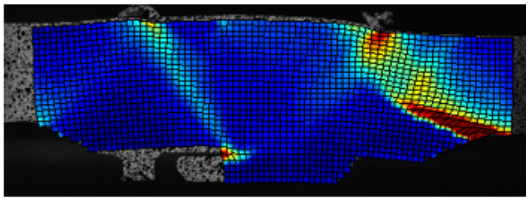

2Gap

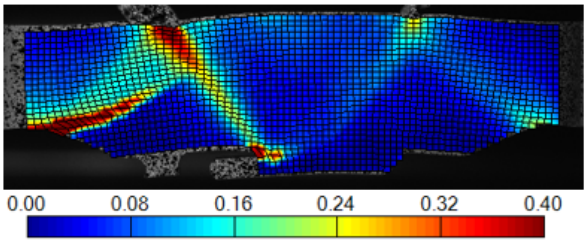

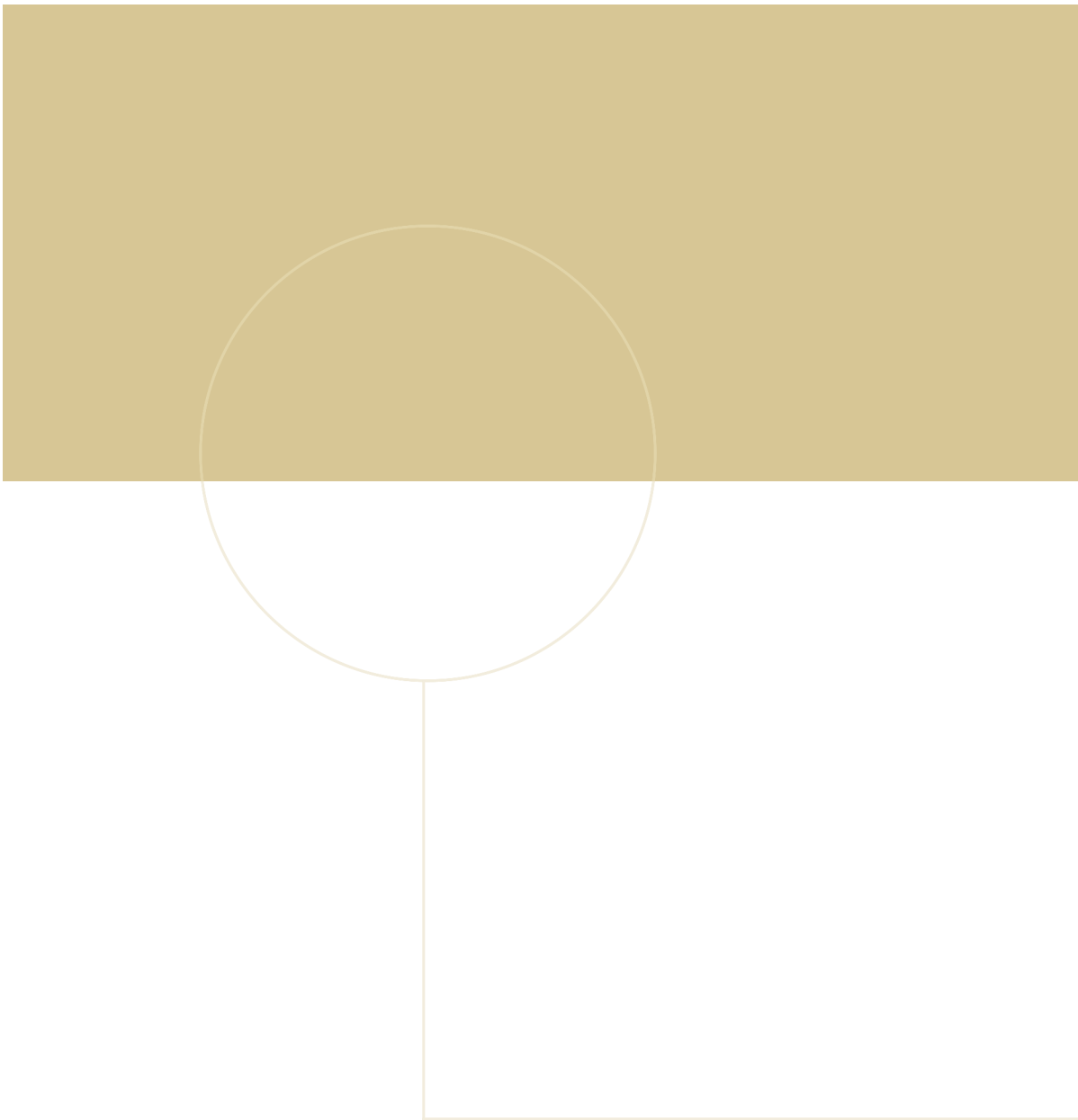

NTNU

Kunnskap for en bedre verden